The Pennsylvania State University

The Graduate School

DEVELOPMENT OF A SPECTROSCOPIC PROCESS MONITORING SYSTEM FOR MULTI-LASER METAL POWDER BED FUSION ADDITIVE MANUFACTURING

A Thesis in

Additive Manufacturing and Design

by

Andrew Przyjemski

Submitted in Partial Fulfillment
of the Requirements
for the Degree of

Master of Science

August 2021

The thesis of Andrew Przyjemski was reviewed and approved by the following:

Abdalla R. Nassar
Head of Process Physics, Analytics, and Engineering Department, and Associate Research Professor, The Applied Research Laboratory
Thesis Advisor

David Corbin
Assistant Research Professor, The Applied Research Laboratory

Timothy W. Simpson
Paul Morrow Professor in Engineering Design and Manufacturing,
Head of the Additive Manufacturing and Design Graduate Program.

ABSTRACT

Multi-laser powder bed fusion additive manufacturing (PBFAM) is the answer to the growing demand for faster and larger part production. However, timely and cost-effective part qualification remains a critical hurdle due to the formation of subsurface flaws during the PBFAM process. Spectroscopic inspired monitoring systems has been shown as a promising technique to detect the presence of flaws using the spectral emissions during the laser welding process. However, the use of spectroscopic sensing in PBFAM systems is complicated by the introduction of multiple simultaneously operating lasers. The work presented in this thesis covers the development of an optical emission spectroscopy inspired, photodiode-based system designed for use in multi-laser PBFAM. The objective of this system is to assist in the real time detection of flaws that form during the PBFAM process.

TABLE OF CONTENTS

LIST OF FIGURES

LIST OF TABLES

ACKNOWLEDGEMENTS

This material is based on research sponsored by Air Force Research Laboratory under agreement number FA8650-20-2-5700. The U.S. Government is authorized to reproduce and distribute reprints for Governmental purposes notwithstanding any copyright notation thereon. The views and conclusions contained herein are those of the authors and should not be interpreted as necessarily representing the official policies or endorsements, either expressed or implied, of Air Force Research Laboratory or the U.S. Government.

I would like to acknowledge my colleagues at CIMP-3D who have been immensely helpful and supportive over the past four years.

I would like to thank my thesis advisor Dr. Abdalla Nassar for being an endless source of guidance, support, and knowledge, and for always pushing me to be a better engineer and scientist.

Finally, I would like to express my deep sense of gratitude to my parents for their unconditional love and support throughout my college career.

Chapter 1

Introduction

Over the past few decades laser powder bed fusion additive manufacturing (LPBFAM) has emerged as an advanced manufacturing method that enables the creation of highly complex components and assemblies not previously manufacturable using traditional methods. This increased design freedom associated with metal additive manufacturing (AM) is made possible through the layer wise nature through which components are fabricated. Beginning with an empty build chamber, a thin (~20-100 μm) layer of powder is deposited across a build plate by the recoating mechanism. The deposited metal powder is then selectively melted using one or more high power laser beams. These lasers are aimed using computer-controlled galvanometers that guide the focus of laser energy along predetermined build paths that together form the geometry of the desired part. This process allows for the creation of complex geometries using a variety of metal alloys. The LPBFAM process is illustrated in figure 1-1.

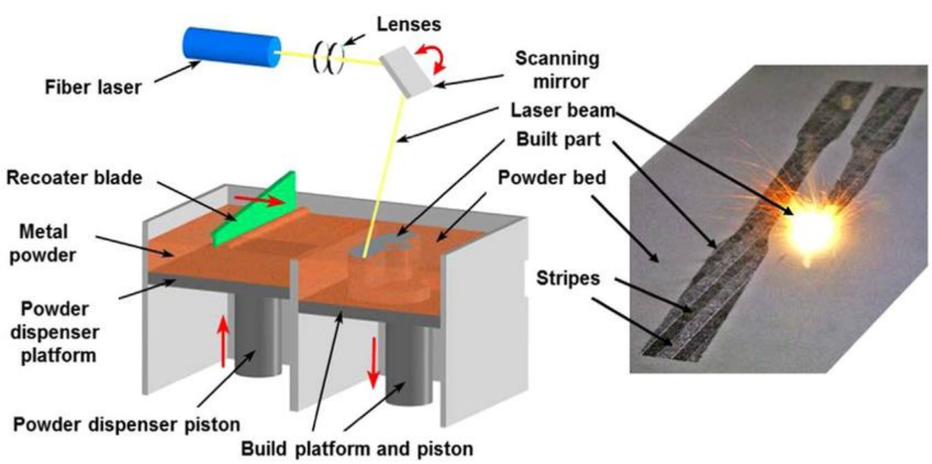

Figure **1-1**: Illustration of the laser powder bed fusion process [1].

While additive manufacturing has had a strong history as being a popular tool for constructing prototype components, a growing trend is the use of metal AM to manufacture end use parts. General Electric has been an industry leader in the push towards high volume metal AM production to mass produce aerospace and medical components. GE has used electron beam melting (EBM) machines produced by Arcam (a subsidiary of GE) to produce over 100,000 titanium hip cups which have been used in hip replacement surgeries around the world. GE has also utilized powder bed fusion additive manufacturing machines produced by Concept Laser (also a GE subsidiary) to produce over 30,000 fuel nozzles for the LEAP engine commonly used in commercial aircraft [7]. An example fuel nozzle produced by GE using additive manufacturing is shown in figure 1-2.

Figure **1-2**: Additive GE fuel nozzle [7].

Using additive manufacturing allowed GE engineers to simplify an assembly which previously consisted of 20 separate pieces welded together to just a single component. This decreases the failure points of the assembly while also reducing the weight of the system by about 25%. It is because of the new manufacturing possibilities afforded by metal AM that the U.S. 3D printing metals market is forecasted to grow at a compound annual growth rate of 32.4% over the next decade [8].

The significant limiting factors preventing the widespread adoption of metal AM for end use part production are the time and cost required to produce and certify manufactured parts. The speed at which parts are created using LPFAM is mostly limited by the rate at which the laser can melt a given material. To satisfy the growing demand for larger and faster part production AM machine manufacturers are developing new multi-laser metal AM systems. New multi-laser systems range the Concept Laser M2 series 5 machines, which include two 1kW lasers capable of simultaneous operation, a nine-laser system being developed under U.S. Army Research Laboratory by 3D systems. While the inclusion of multiple lasers allows for faster material processing, it does not solve the issue of part qualification.

Figure **1-3**: Concept Laser M2 Series 5 [9].

During the laser fusion process, defects can form because of many different variables such as material contamination, melt pool instability, part deformation, laser power fluctuations or other processing variables [2]. Often, the presence of these flaws cannot be easily detected and can result in poor mechanical properties [4]. In applications such as aircraft components or biomedical implants, it is critical that parts are properly certified for use. Often this certification involves using computed tomography (CT) scanning to identify subsurface part defects that can lead to a degradation in part performance. However, the process of CT scanning metal AM components is a time consuming and costly process which often makes it cost prohibitive for use in qualifying end use parts.

To solve this issue many researchers have investigated the use of in-situ processing monitoring to assist in defect detection to pave the way for real time part qualification. The process monitoring sensors used in metal AM machines typical measure acoustic, spectral, or thermal emissions during the laser welding process [10]. Of the process monitoring techniques that exist, optical emission spectroscopy (OES) has emerged a prominent technique to correlate the spectral emissions from the plasma plume created during the laser welding process to the presence of build defects. Prior research has shown that spectral emissions from the plasma plume can be used to identify the presence of lack-of-fusion and keyhole defects [11].

An OES sensor in a metal PBFAM system is typically setup in an off-axis arrangement where the sensor field of view (FOV) encompasses the entirety of the machine build plate. The accurate sensing of the plasma plume using this arrangement in multi-laser systems is complicated by the inclusion of multiple simultaneously occurring plumes. The work presented in this paper aims to solve this problem through the development of an on-axis OES inspired sensor system capable of identifying process related defects in multi-laser PBFAM systems. The goal of this research is to introduce new technology and methods that can be used towards the goal of real time part qualification in metal AM systems.

Chapter 2

Literature Review

Many different process monitoring sensors have been developed to inform about the quality of the laser welding process. These sensors typically measure one or more melt pool attributes, such as geometry [12], temperature [10], or spectral emissions to determine weld quality [13]–[18]. This method of in-situ sensing is intended to provide a means to qualify parts in real time, eliminating the need for time intensive and costly post-process analysis [19].

Spectroscopy is an attractive option for laser welding process monitoring due to low cost and high sampling rates of spectroscopic process monitoring sensors [20]. Previous implementations of spectroscopic systems to monitor the welding process in both arc and laser based welding systems has shown the capability of such systems to detect the presence of trapped gas porosity and lack-of-fusion defects [2], [21], [22]. Additionally, spectroscopy systems have been shown to provide the ability to monitor melt pool depth during the laser welding process [23]. Spectroscopic systems for LPBFAM machines are designed to collect data on the spectral emissions from the plasma plume generated during the laser welding process. This data can be processed to identify the formation of flaws in real time and allow for corrections to be made [16], [23]. These sensing methods typically employ either photodiode-based or spectrometer-based sensor systems to monitor spectral line and background radiation emitted by the plasma plume. The line and background emissions have been shown to be useful in determining the presence of defects in laser-based metal additive manufacturing [2], [3], [11], [24]. This shows that the plasma plume formation provides a means to understand the laser welding process. Spectroscopic methods can be used to provide a deeper understanding of the physical connection between the plasma plume formation and defect formation mechanisms.

During the LPBFAM process, laser energy is directed at metal powder which in turn absorbs some of this energy. If sufficient energy is absorbed, the material becomes a liquid. If sufficiently more energy is absorbed the material evaporates forming a vapor. During the LPBFAM process this is shown through the formation of a liquid melt pool and a metallic vapor centered around the laser focus. Further absorption of laser energy by the vapor cloud causes electrons to be stripped from atoms, forming an ionized plasma as shown in figure 2-1 [25].

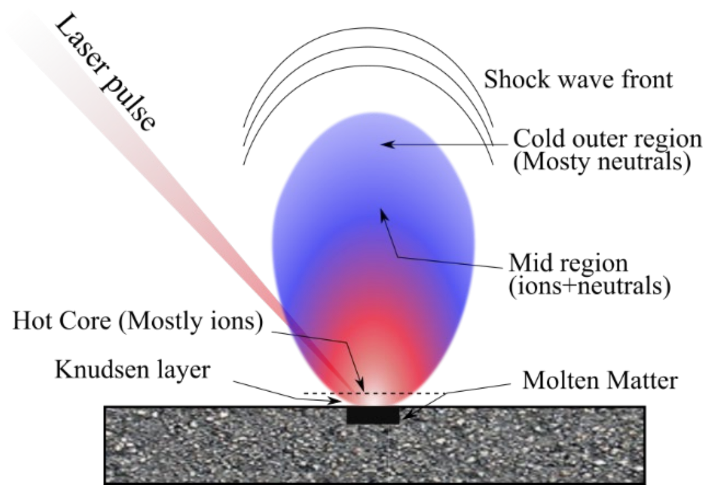

Figure **2-1**: Laser induced plasma formation [26].

It is the spectral emissions from this plasma that have been shown to yield meaningful process related data [3], [11], [24]. Radiation is emitted by the plasma through three different radiation emission mechanisms: bound-bound, free-bound, and free-free electron transitions [27]. Bound-bound transitions occur when an electron moves from one discrete energy level to another. When an electron decays from a higher orbit to a low orbit energy is conserved through the emission of a photon with a wavelength given by Planck's equation (Eq (1), where ΔE is the energy difference between levels, $h \approx 6.626 \times 10^{-34}$ m^{2}kg/s is Planck's constant, and ν is the emitted photon frequency.

$$\Delta E = hv \tag{1}$$

An atom for a given element has a unique set of energy levels corresponding to a unique set of wavelengths likely to be emitted from bound-bound transitions. These narrow bands of discrete wavelengths are known as characteristic emission lines and vary from material to material depending on the underlying elements that comprise it. Free-bound transitions occur when a previously unbound electron is capture by an ion and assumes an energy level. This process is known as radiative recombination and results in the emission of a photon in congruence with of the conservation of energy. When in the free state, electron energy is not defined as discrete levels as it is in the bound-bound case. Instead the electron energy is kinetic. This results in the emission of photons without discretely defined wavelengths as in the bound-bound case. This type of emission is observed as continuum radiation. The last type of transition is free-free where the energy level of an electron changes through the absorption or emission of photons. The process by which a free electron absorbs a photon is known as Inverse Bremsstrahlung absorption. In the reverse case, Bremsstrahlung radiation is emitted if an electron is slowed, for instance when deflected by an atomic or ionic nucleus. Again, this type of radiation does not result from discrete energy level transitions and therefore contributes towards continuum radiation. The resulting spectral radiation emitted by the plasma plume can be seen as the superposition of the emission lines from the bound-bound transitions, and the continuum radiation given off by the free-bound and free-free transitions. Because each element has a unique set of energy levels, each element will have a unique radiation curve. As such, during PBFAM, processing different materials will generate different spectral signatures.

The emission lines and background radiation emitted by the plasma plume serve as foundation for most spectroscopic weld monitoring methods. One such method has been to use the relative line intensities from the same element to calculate the electron temperature of the plasma. Equation (2) shows the relationship between the relative line intensity ratio R and the electron temperature T_e [27].

$$R = \frac{I_1}{I_2} = \frac{A_1 g_{m1} \lambda_1}{A_2 g_{m2} \lambda_2} exp\left(\frac{E_{m2} - E_{m1}}{kT_e}\right) \tag{2}$$

Where I_1 and I_2 represent the relative line intensities, A_1 and A_2 are the transition probabilities, g_{m1} and g_{m2} are the statistical weights, λ_1 and λ_2 are the wavelengths, and E_m represents the respective excitation energies. This equation can be rearranged into Equation (3) to provide an expression for the plasma electron temperature.

$$T_e = \frac{E_{m2} - E_{m1}}{k \ln \frac{I_1 A_1 g_{m1} \lambda_1}{I_2 A_2 g_{m2} \lambda_2}} \tag{3}$$

Research by Ancona et al. showed that after varying processing parameters the best results were obtained when the variation in electron temperature was low, indicating that a higher standard deviation in electron temperature corresponded with the presence of weld defects [19]. Ancona also demonstrates that local decreases in electron temperature indicate the presence of weld defects. The use of the plasma electron temperature is not solely limited to defect detection. Research by Sebestova et al. has shown that there is correlation between the plasma electron temperature and the weld penetration depth [12]. Because the electron temperature calculation method requires the measurement of two separate emission lines as well as the continuum radiation needed to perform a background subtraction, a spectrometer is typically employed to perform the measurements.

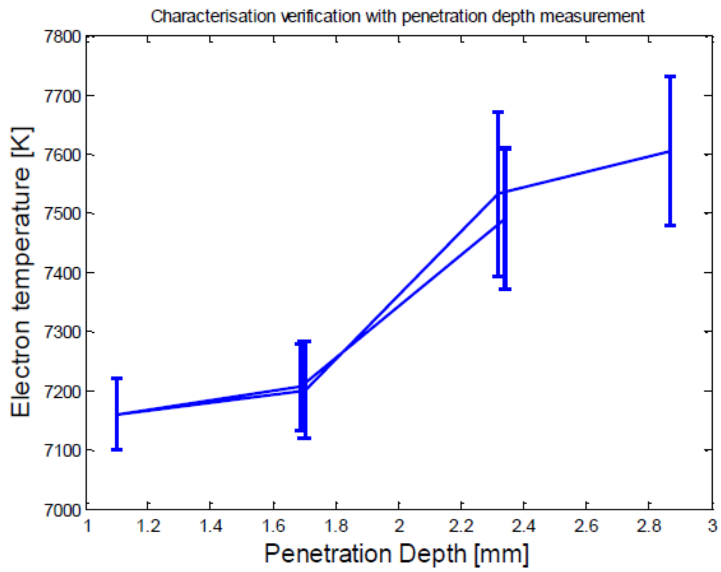

Figure **2-2**: Relationship between electron temperature and weld penetration depth [12].

An alternative approach that has previously been demonstrated is to simply use the ratio of a particular emission line to the background continuum as a metric to detect the formation of flaws during the LPBFAM process. An illustration of the line and continuum radiation is shown in figure 2-3. The advantage of this method over the aforementioned electron temperature calculation method is the reduction in computational power required to perform real time analysis [28].

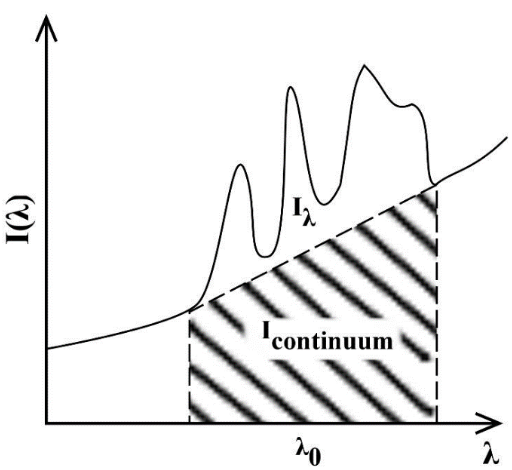

Figure **2-3**: Illustration of line (I_λ) and continuum ($I_{continuum}$) radiation. Adapted from [2].

This method was used by Garcia-Allende et al. to detect the presence of flaws induced during the arc-welding process. Their analysis covers multiple different emission lines and shows a strong correlation between the occurrence of flaws and sharp changes in the line-to-continuum ratio. Research by Nassar et al. employed a similar line-to-continuum measuring method applied to the directed energy deposition (DED) process which shows the occurrence of defects correlating with fluctuating line emissions [2]. Additionally their research shows a correlation between the line-to-continuum ration and the presence of lack of fusion defects between hatches. This relationship is shown in figure 2-4.

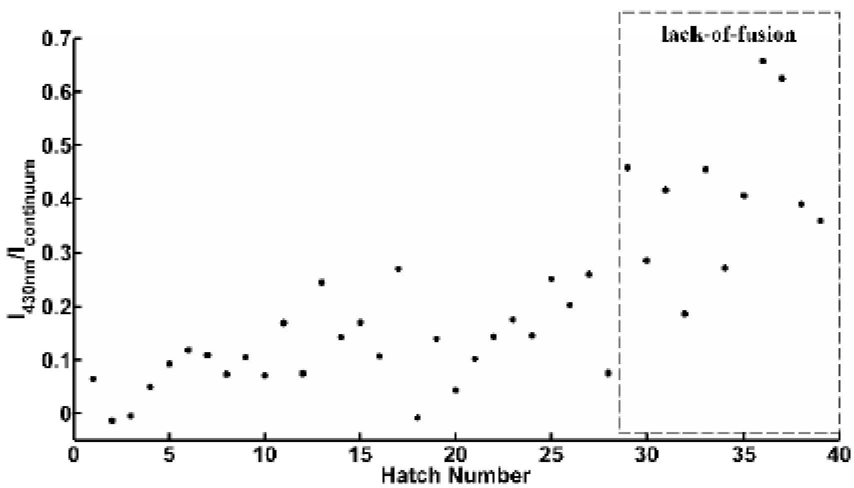

Figure **2-4**: Relationship demonstrated between the line-to-continuum ratio and the presence of lack-of-fusion defects in directed energy deposition as shown by Nassar et al. [2].

Typically a spectrometer is employed to collect spectral data, however an alternative method is to use a limited number of photodiodes with optical filters corresponding to the desired emission lines and continuum zone. Research by Mirapeix et al. compared the use of a spectrometer vs. a photodiode arrangement in an arc-welding system and concluded that the photodiode system provides an improved signal to noise ratio at a significantly lower cost compared to the spectrometer approach [29]. A similar approach developed by Dunbar et al. used a two photodiode arrangement in an off-axis configuration where one photodiode is filtered to observe a prominent emission line and the other is filtered to observe the continuum radiation [3]. This setup was deployed in a PBFAM system and showed the relationship between the line-to-continuum ratio and the percent void in as built components. This setup is shown in figure 2-5.

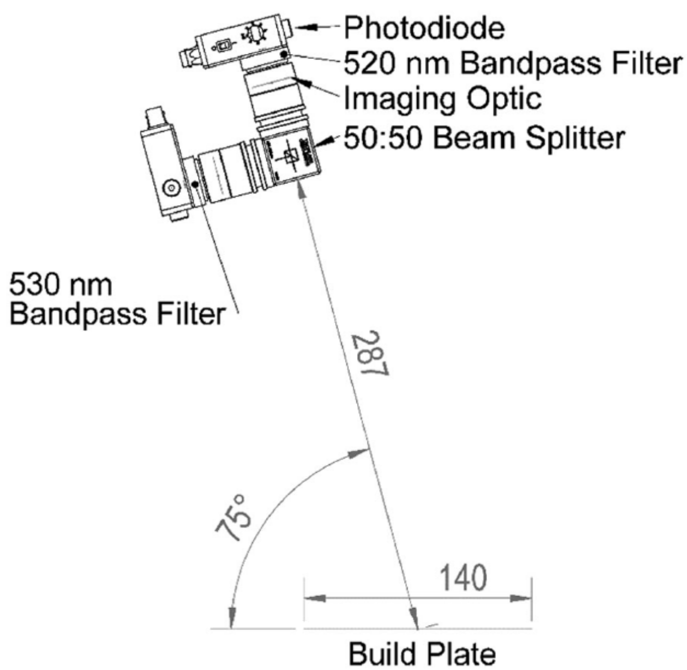

Figure **2-5**: Off-axis photodiode arrangement developed by Dunbar et al. [3].

Despite research empirically showing a link between plasma spectral phenomena and the occurrence of flaws in LPFAM, the physics behind this connection is still not completely understood. However, the mechanisms by which flaws form during the laser welding process is widely understood and can provide valuable insight into how spectroscopy can be used to identify the formation of different types of flaws. Defects arise in LPBFAM components often due to an imbalance in processing parameters, however even under ideal processing conditions stochastic flaws can occasionally form without any obvious causes [4]. Figure 2-6 shows how flaws can be categorized as either systemic meaning that the formation is linked to the processing parameters, or stochastic indicating random formation.

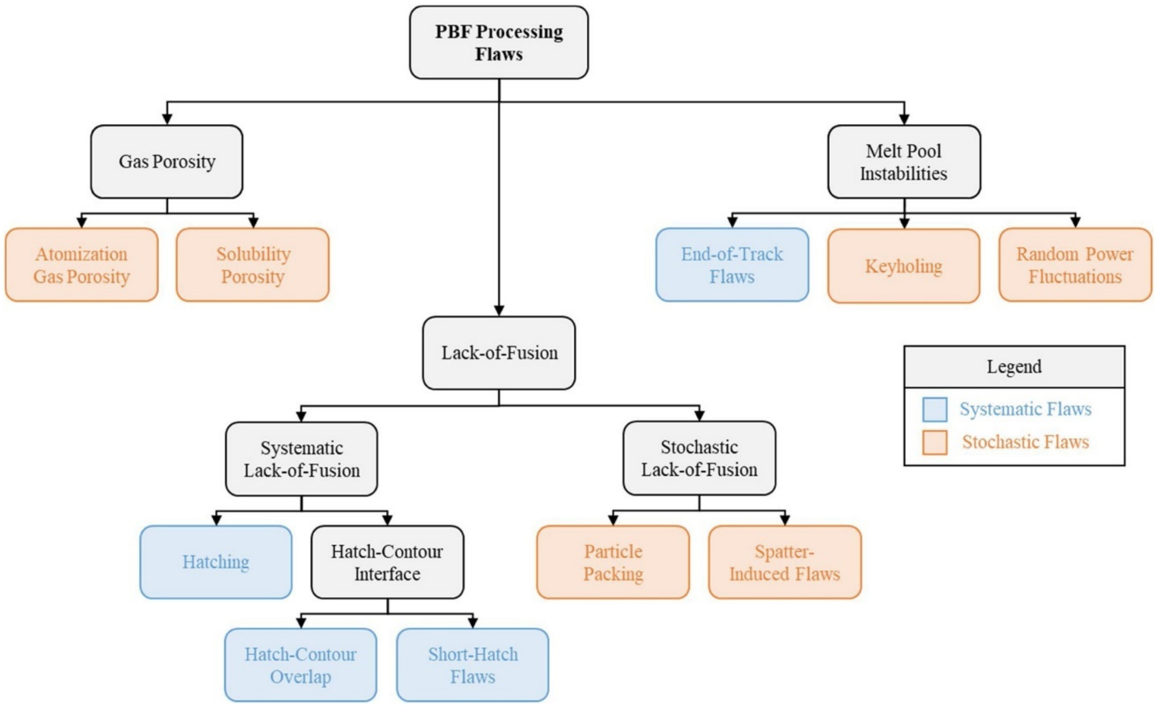

Figure **2-6**: Common defect categories for laser powder bed fusion additive manufacturing. Adapted from [4].

In this diagram, flaw types such as systemic lack-of-fusion defects are typically the result of improper path planning or process parameter selection. Keyhole defects forming during laser keyhole welding are a commonly studied flaw type due to the ease at which keyhole defects can be elucidated during the welding process. Process parameters can be purposely set to elicit the formation of keyhole defects, allowing for this formation mechanism to be more easily studied. Keyhole welding occurs when there is sufficient laser energy to cause material to evaporate to the extent that a depressions, deeper than the half-width of the weld, which is stabilized by the vapor pressure generated during evaporation [25]. This forms a keyhole shaped weld that penetrates deeper into the substrate. Laser energy entering the keyhole will reflect off the sloping leading edge of the keyhole and be absorbed into the melt pool. This results in nearly all the laser energy being absorbed by the melt pool. Research by Katayama et al. has shown that the intense vaporization that occurs during the keyhole welding process will result in the formation of vapor bubbles in the melt pool which may become trapped as the material solidifies [30]. This formation mechanism is summarized in figure 2-7.

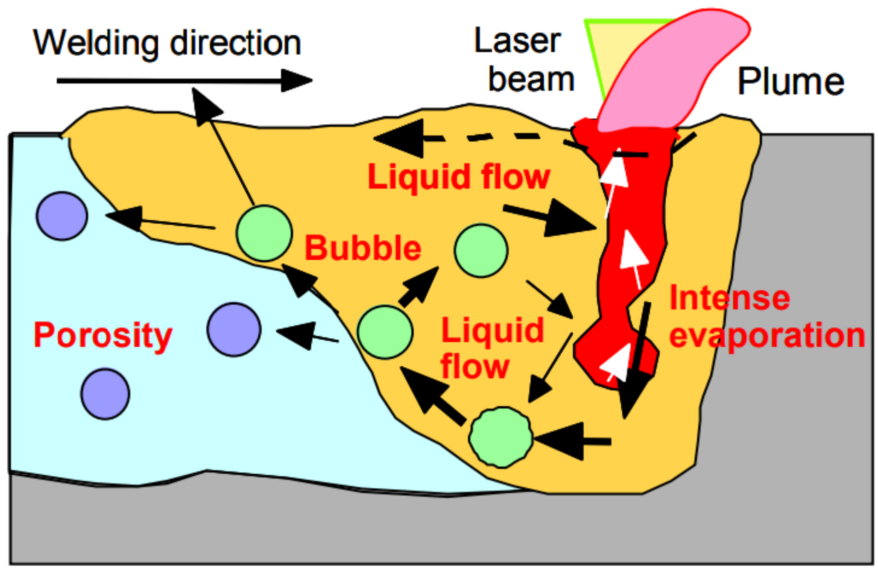

Figure **2-7** Laser keyhole welding and keyhole defect formation diagram. Adapted from [5].

Because the formation of keyhole induced porosity initiates within the liquified melt pool the resulting trapped vapor bubbles will form spherical defects. Because of this, keyhole defects are often identified by their characteristic spherical shape.

As discussed above, the plasma spectral phenomena that occurs during LPBFAM process provides real time analytics which can be used to identify defects in as-built components. The objective of this work is to build upon this foundational knowledge to develop and validate an optical emission spectroscopy-inspired system capable of measuring plasma plume emissions and identifying defects in multi-laser PBFAM.

Chapter 3

On-Axis Multi-Spectral Sensor Development

3.1 Objective

The primary objective of the spectral sensor developed herein was to measure the radiation emitted from the plasma plume created during the laser welding process. The system must also be able to operate in a multi-laser PBFAM machine which requires independent monitoring of multiple, simultaneously occurring plasmas. The follow sections detail the critical design elements incorporated into the proposed spectral sensor to achieve these objectives.

3.2 Optical Design

Process monitoring sensors employed in a PBFAM system are typically configured in an off-axis arrangement where the entirety of the build plate is imaged by the sensor. In a multi-laser PBFAM system this type of sensor arrangement is non-ideal due to the inability to distinguish between the signals measured from each melt pool. To allow for the monitoring of multiple, simultaneously occurring melt pools an on-axis sensing approach was employed. This method allows the spectral sensor to utilize the existing optical train of the PBFAM system to image only the area directly around the melt pool. In this configuration light emitted from the plasma plume travels back through the laser path, reflects off both galvanometer mirrors, before then passing through the laser focusing optics and passing through a dichroic mirror designed to reflect the laser wavelength and transmit all other wavelengths. After passing through the dichroic mirror, the light is collected by the spectral sensor. This sensing approach is illustrated in figure 3-1.

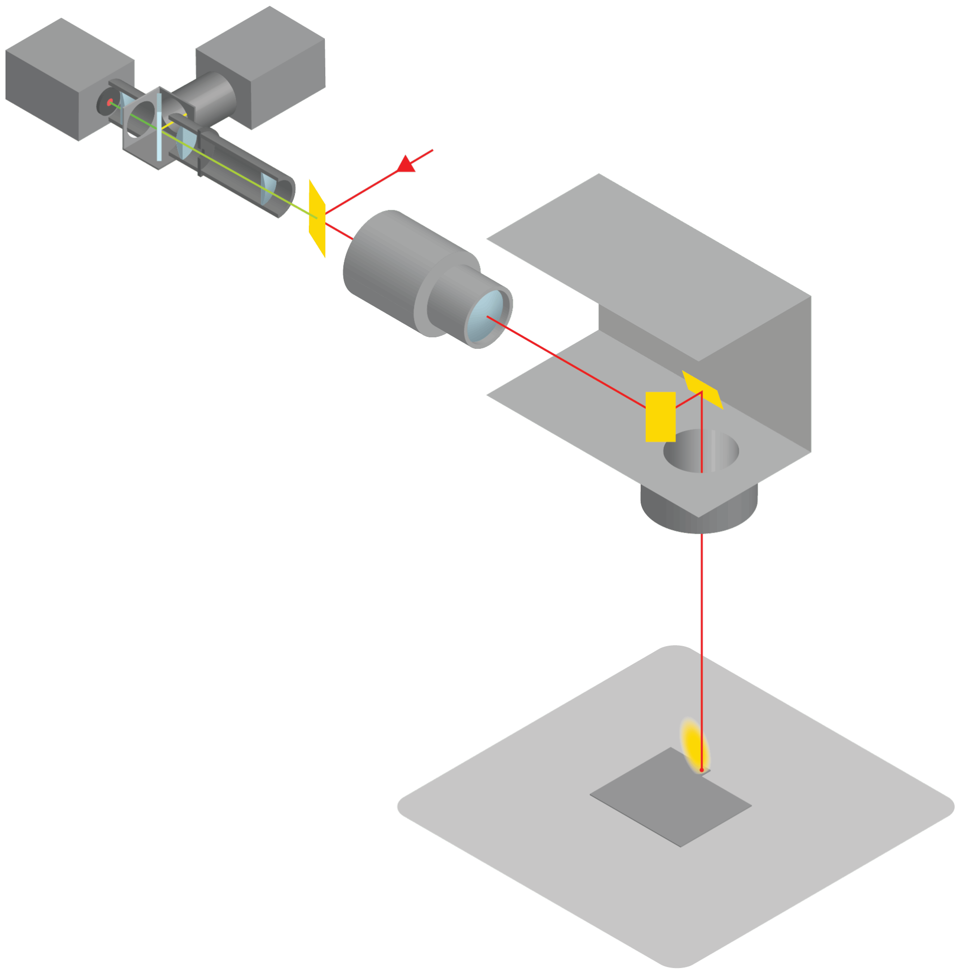

Figure **3-1** On-axis sensing approach

The size of the object that can be imaged by the sensor is limited by the field stop which is an optical parameter of the sensor system. The imaging size of the sensor, otherwise known as field-of-view (FOV), can be controlled by the operator by introducing a variable aperture iris into the system. This type of control is advantageous as it allows the operator to fine tune the FOV of the sensor to reduce the chance of interference from other plasma plumes. However, due to the long focal length of the overall system, the minimum iris size required to have meaningful control over the FOV would have to be on the order of 0.1mm. Achieving this diameter in practice is impractical as adjustable aperture iris's typically have a minimum diameter on the order of 1mm.

Additionally, diffraction effects become more significant as the aperture diameter is lowered, so it is desirable to have a higher aperture diameter. To obtain a proper balance between FOV control and abiding by practical limitations optical elements were introduced into the design to elongate the distance between the focusing element and the field stop. This design allows a larger aperture iris to be used while still allowing for significant control over the sensor FOV. This arrangement is illustrated in figure 3-2.

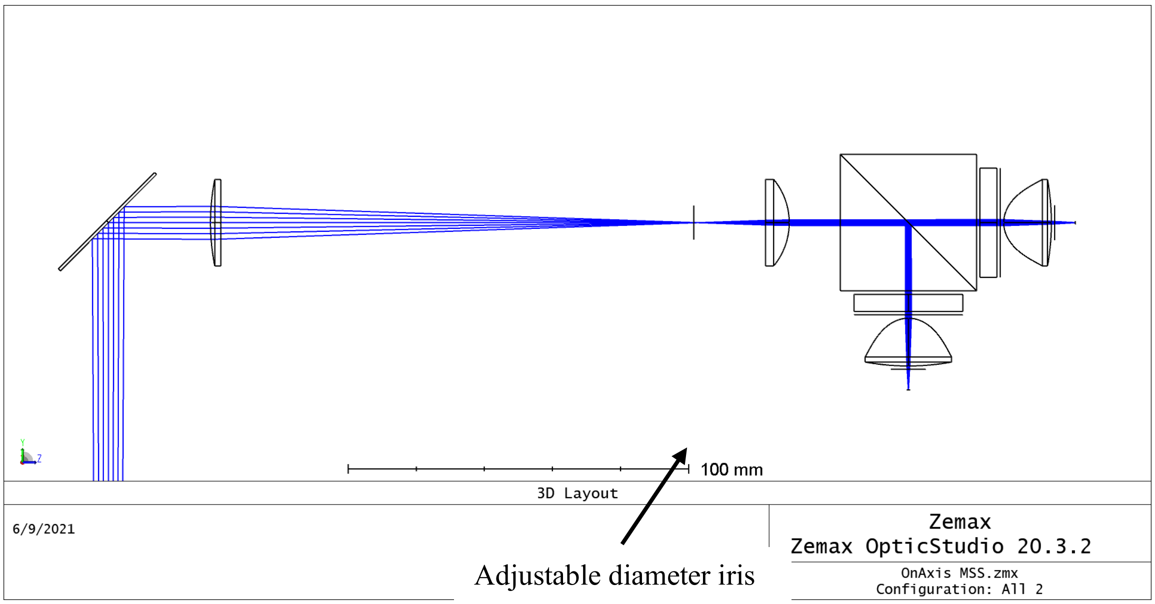

Figure **3-2** Sensor optical design with adjustable aperture element

The selected iris has a diameter that is adjustable between 0.8 and 12mm. The effect this diameter has on sensor field of view is shown in figure 3-3. In this plot field-of-view refers to the maximum size object that can be imaged by the sensor.

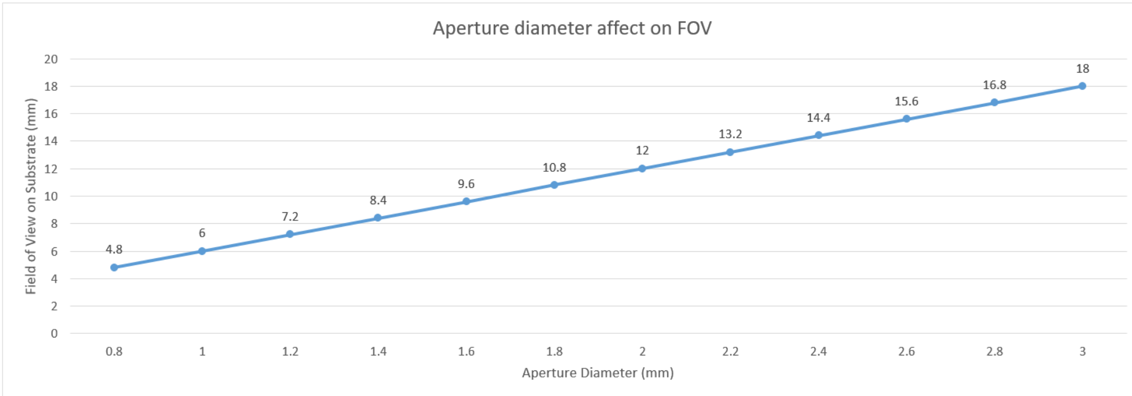

Figure **3-3** Sensor field-of-view for varying aperture diameters

After passing through the field stop, the light must be separated into its line and continuum components. This is done with a beam splitter and bandpass filter combination which effectively splits the beam of light into two different beams that are subsequently filtered down to the desired wavelengths. These two beams of filtered light are then focused onto the sensor plane of their respective photodiodes which are used to record the intensity of light. This arrangement is illustrated in figure 3-4.

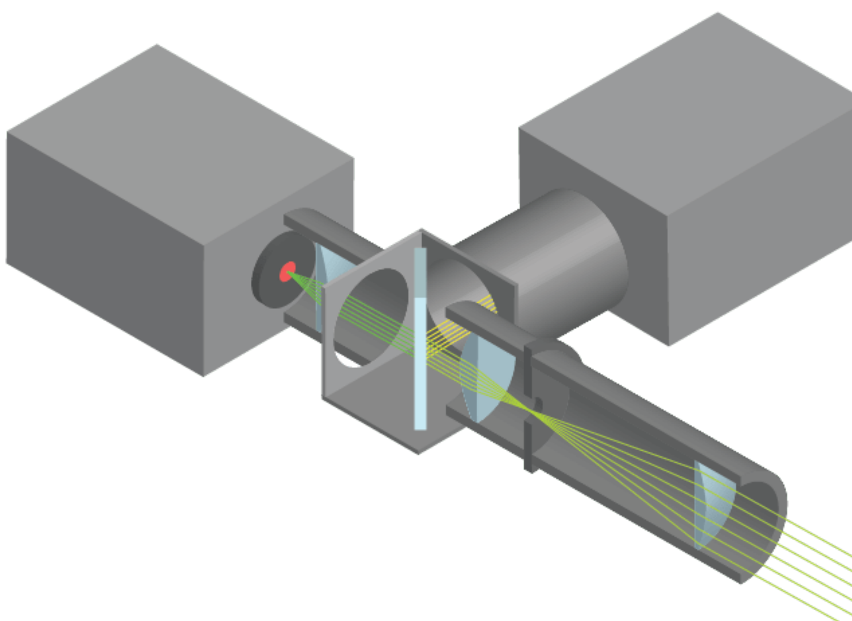

Figure **3-4** Spectral sensor assembly with eamsplitter and optical filter arrangement

One of these photodiodes is set to monitor line emissions from the plasma plume and is thus designated the line photodiode. The other photodiode is set to monitor the continuum emissions from the plasma plume and is thus designated the continuum photodiode. In this setup the optical bandpass filters used to isolate the respective line and continuum wavelengths are a critical element of the system and must be properly selected to provide effective monitoring of the laser welding process. The wavelength of these filters is determined by line spectrum for the material that is being processed. The sensor system developed herein is designed to monitor the laser welding of the popular titanium alloy Ti6Al4V for which the line spectrum plot is shown in figure 3-5.

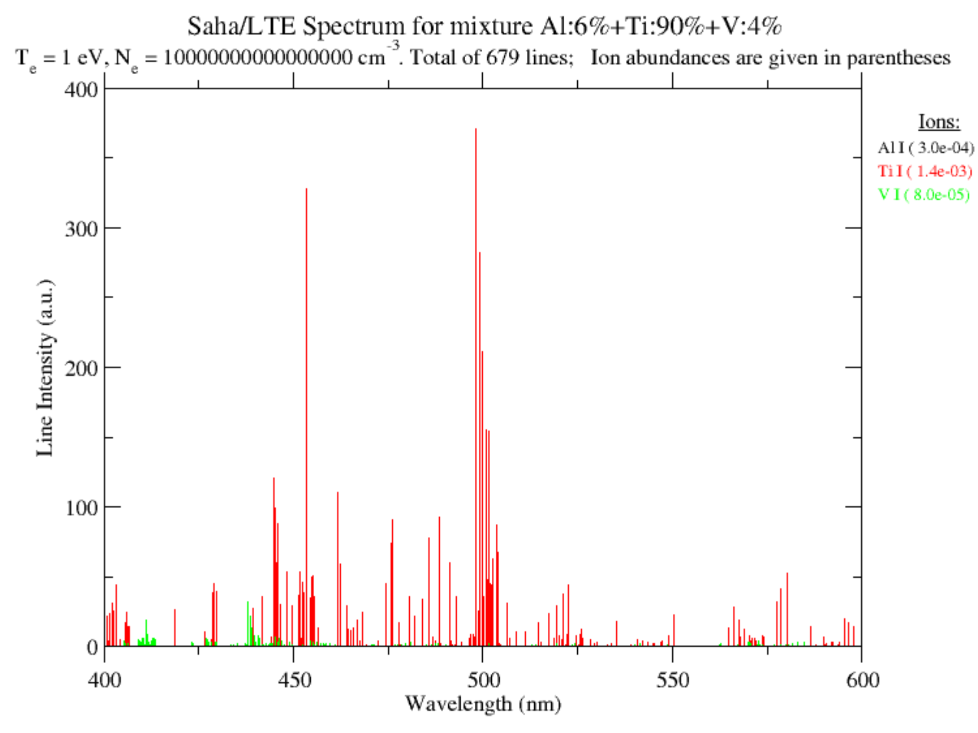

Figure **3-5** Line spectrum plot for Ti6Al4V [6].

As the name suggests, the line photodiode is intended to be filtered to a wavelength corresponding with high intensity lines for the base material. The continuum photodiode, on the other hand is intended to be filtered to a wavelength corresponding with a lack of high intensity lines to only capture the background radiation. Based on these principles a reasonable selection for the line wavelength filter would be 500 nm which corresponds with a region of high intensity lines for titanium. However, before the photodiode wavelengths are selected, other optical intensity losses associated with the optical system must be considered. A critical area of intensity loss is the galvanometer mirrors. The coatings for these mirrors are designed to reflect nearly all light at the laser wavelength, but the reflectivity at other wavelengths is often much worse. Additionally the galvanometer mirrors rotate to change the position of the laser beam and this rotation changes the angle of incidence (AOI) for which light strikes the mirror. If the mirror reflectivity is not constant across a varying AOI then there will be spatial variations in sensor signal that must be considered. A spectrophotometer was employed to analyze a set of galvanometer mirrors to determine effect of incidence angle and wavelength on mirror reflectivity. The results from this analysis are shown in figure 3-6.

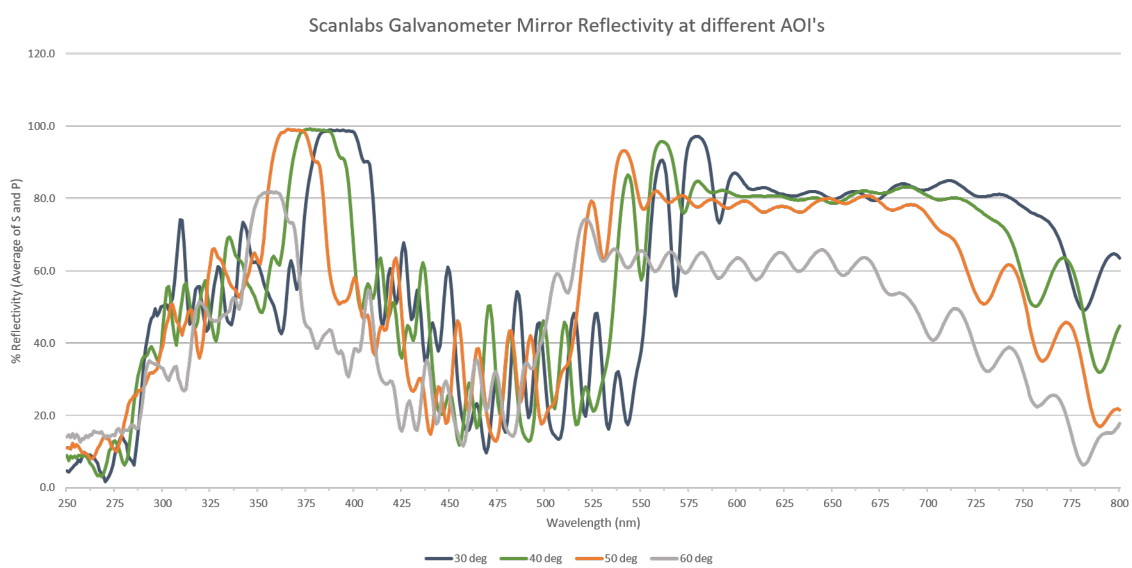

Figure **3-6** Galvanometer mirror reflectivity analysis.

The spectrophotometry data shows that mirror reflectivity can vary significantly based on AOI and that reflectivity is poor between 400 – 550 nm. The variation in intensity due to AOI shows that there will indeed be a spatial variation in spectral intensity. The method to compensate for this spatial variation is detailed further in the following chapter. To determine which spectral lines are the best candidates for analysis, the mirror reflectivity was averaged and multiplied by the spectral line intensities for titanium. The scanner mirror reflectivity data averaged across all AOI's is shown in figure 3-7.

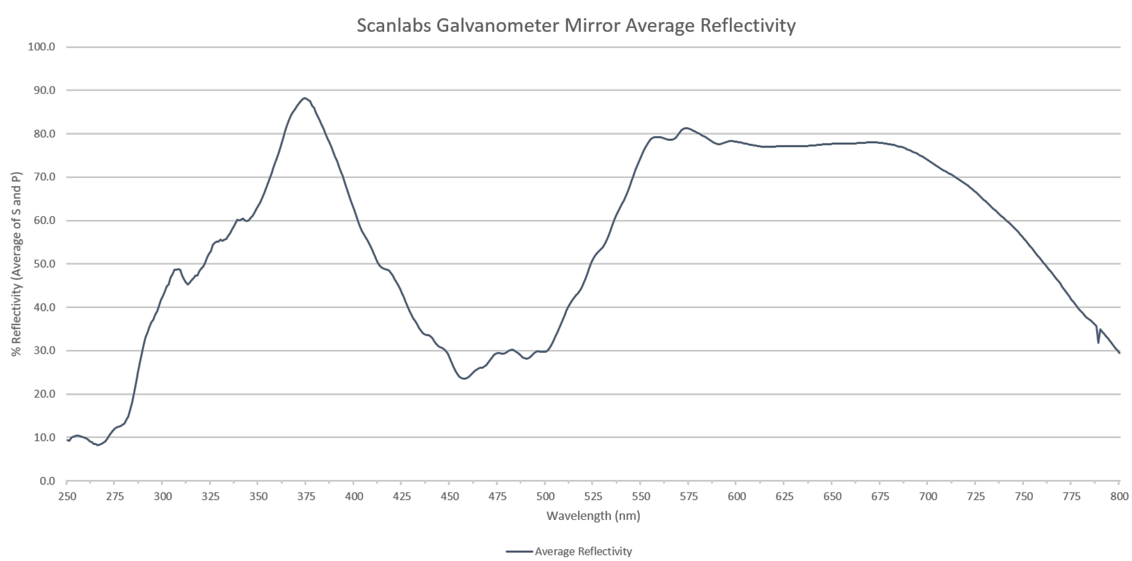

Figure **3-7** Galvanometer mirror reflectivity averaged.

Multiplying this reflectivity data as a percentage of max reflectivity with the line intensity data gathered from NIST yields the relative line intensity plot shown in figure 3-8. This analysis was only performed for the titanium emission lines as the aluminum and vanadium lines in Ti6Al4V are very weak compared to titanium.

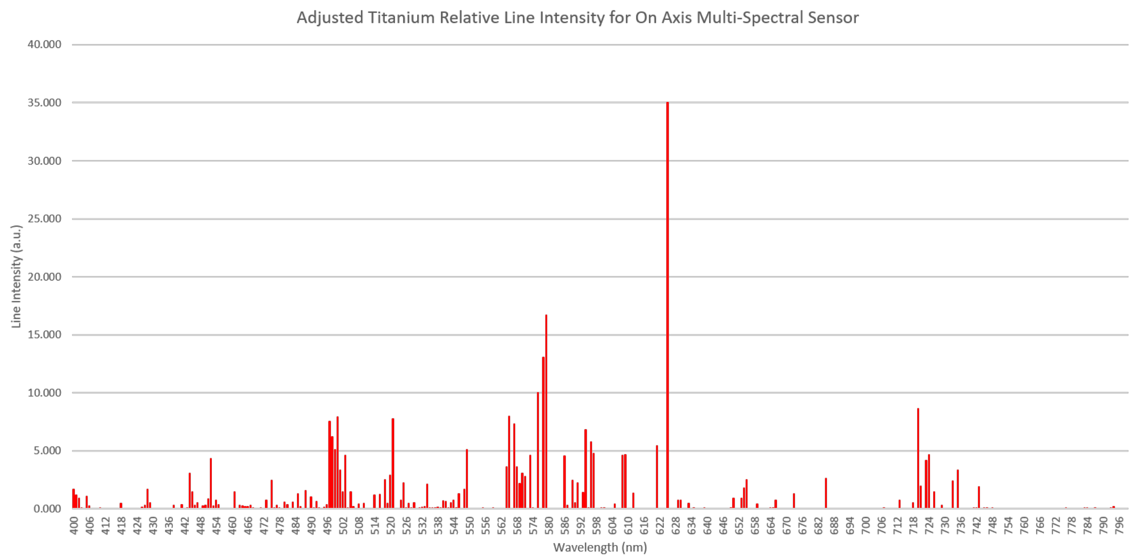

Figure **3-8** Relative line intensity plot for titanium.

From this relative line intensity data the center wavelength (CWL) for the line photodiode filter was selected to be 580 nm due to the cluster of medium intensity lines at that region. The CWL for the continuum photodiode was selected to be 560 nm due to the absence of emission lines at that region. Both filters were selected to have a full width half maximum (FWHM) of 10 nm.

3.3 Hardware Design and Installation

The main constraint with the hardware design of the spectral sensor was the size limitations dictated by the available space in the designated PBFAM machine. For this project, the end machine was a Concept Laser M2 machine. The final hardware design to encapsulate the optical elements required is shown in figure 3-9.

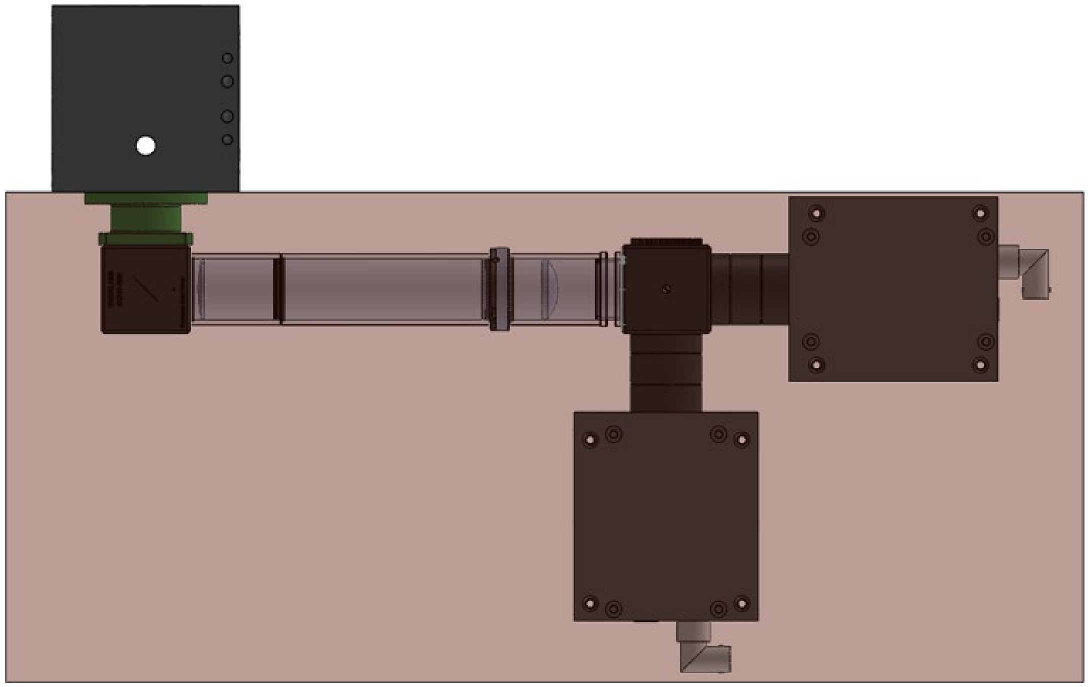

Figure **3-9** Spectral sensor hardware design.

This design includes a custom machine mount shown in green to interface between the spectral sensor and the available mounting fixture on the Concept M2. A fold mirror is located at the start of the optical path of the sensor to ensure that the sensor system fits within the bounding box dictated by the Concept M2 which is shown in red. The two photodiodes are shown as the rectangular gray boxes on the righthand side of the figure. The photodiodes used were C12703-01 avalanche photodiodes from Hamamatsu. Avalanche photodiodes exhibit high sensitivity which makes them an ideal candidate for sensing in low light conditions. The final installed spectral sensor assembly is shown in figure 3-10.

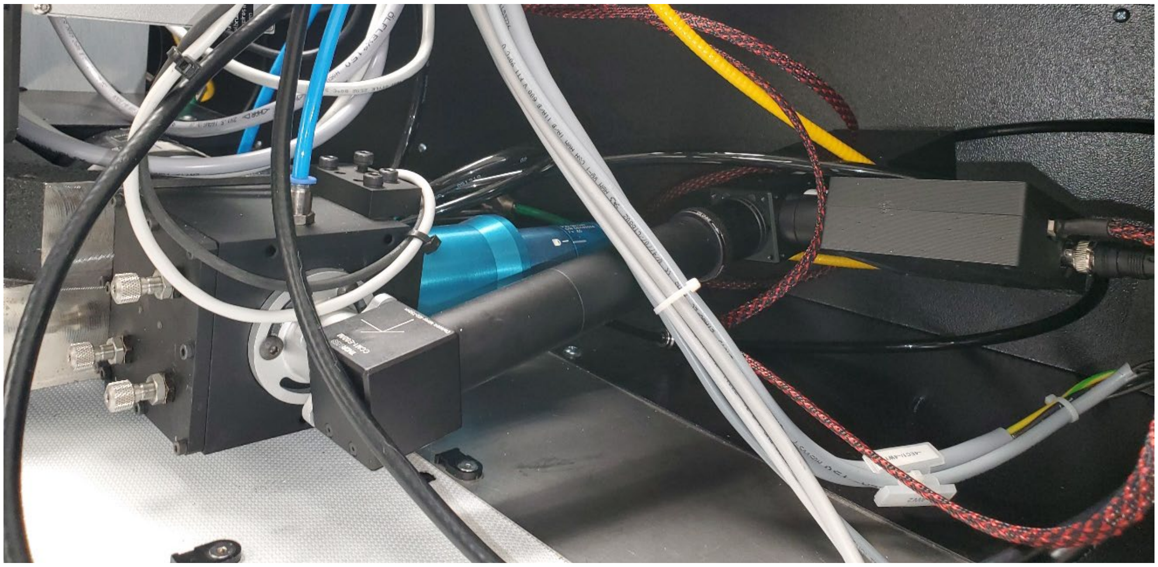

Figure **3-10** Spectral sensor installation.

Because the Concept Laser M2 system is a two-laser machine, two identical spectral sensors were built and installed on the M2's respective scanner systems.

Chapter 4

Multi-Spectral Sensor Calibration System Development

4.1 Objective

The primary objective of the spectral sensor calibration system is to provide a means to correct for the spatial variation in spectral response. As previously mentioned, the position of the laser beam on the build plate is controlled by the angle of the galvanometer mirrors. As shown, the angle of these mirrors has a significant effect on how much light reaches the spectral sensor. This effect results in a spatial variation in spectral intensity independent of the light source intensity. The calibration system was developed to use a light source of a known and constant intensity to quantify the spatial variation in spectral intensity and correct for it. Additionally, the calibration system also has secondary objective to serve as a test bed for using other sensors within a PBFAM system.

4.2 Calibration System Design

To collect accurate calibration data, it is required that the calibration system be capable of moving a source of light of a known intensity across the processing zone of the PBFAM system. In this situation the light source can be seen as an analog for the light emitted from the plasma plume during the laser welding process. To mimic processing conditions a 3-axis stage system was designed to fit within the processing bay of the Concept M2 and traverse a light bulb around the processing plane. The three axes consist of two stepper motors that move the end effector of the stage in a 2D plane and an additional stepper motor that provides additional movement in the same plane. This kinematic approach was chosen as it maximizes the reachable area of the end effector. Due to the size constraints dictated by the size of the processing bay, a two-axis system alone would not be capable of covering a significant area of the processing plane. The addition of a third rotational axis allows the end effector to extend beyond the reach of the two-axis system alone. This kinematic design is shown in figure 3-11.

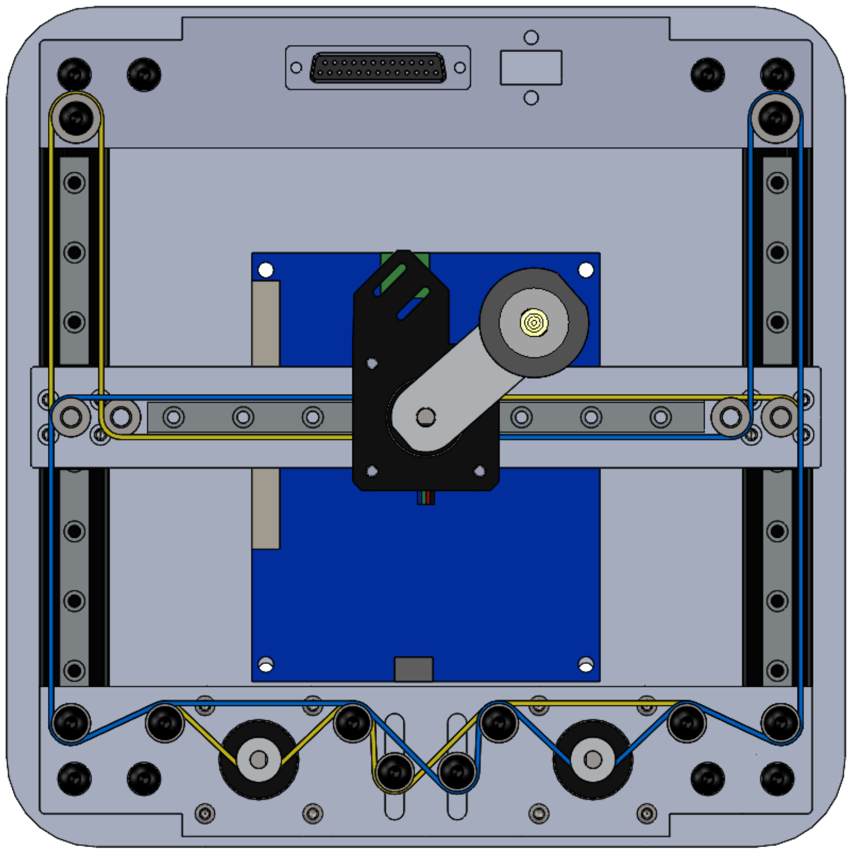

Figure **4-1** Calibration stage mechanical design.

To further mimic the processing conditions in which a plasma plume is formed, a magnetic coupling system was designed to physically separate the light source from the stage mechanics. This method incorporates a flat aluminum panel which serves as a barrier between the magnet connected to the stage mechanics and the magnet mounted to the light source. This ensures that only the light source and the aluminum plate are exposed which provides a good analog for the processing conditions. Figure 3-12 shows the final stage system located in the

Concept M2 processing bay. The light source used during calibration is a tungsten bulb which emits a continuous spectrum of light from 300nm to 1400nm.

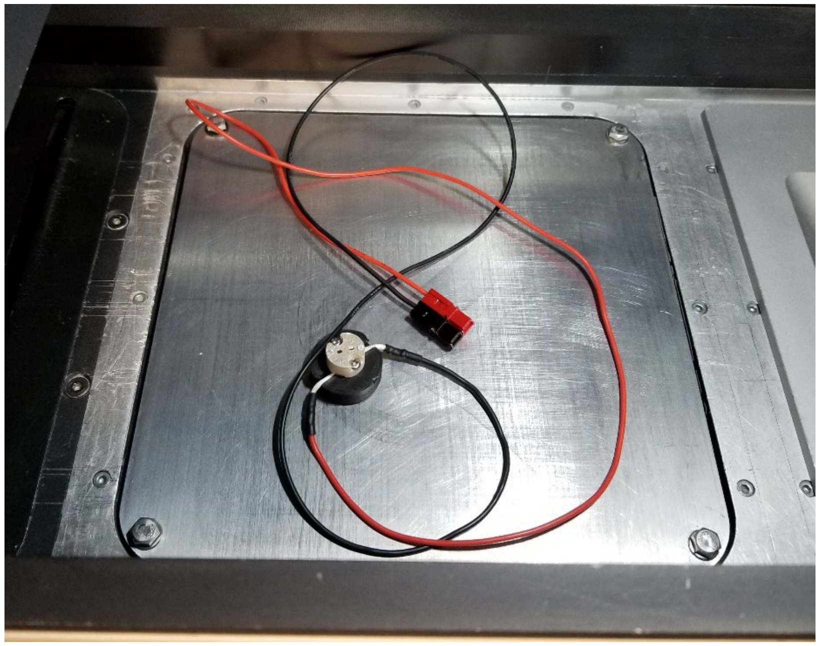

Figure **4-2** Stage system placed in the Concept M2 processing bay.

Because the stage system is in the processing bay of the machine during testing, side panels were incorporated into the design to shield the inside electronics from any leftover metal powder that may be present. The final design with improved dust proof design is shown in figure 3-13.

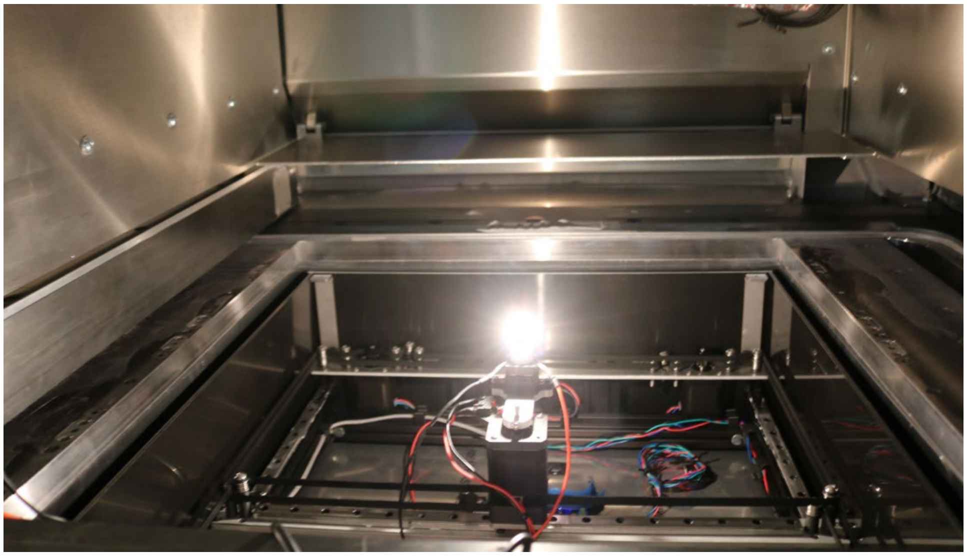

Figure **4-3** Stage system with top cover removed placed in a processing bay.

To control the stage movement, all three stepper motors and corresponding limit switches are connected to a Duet 2 control board, a popular choice for desktop 3D printers. Using the Duet allows for the control of the stage system over USB via G-code commands. These commands are sent from the LabVIEW stage control software shown in figure 3-12. The responsibility of the stage software is to generate a 2D grid of points and move the light source from point to point, collected spectral data at each location. Because the FOV of the spectral sensors are limited to the immediate area around where the laser scanner is aimed, this requires position coordination between the stage system and the Concept M2 system. This was completed using a TCP/IP connection established between the stage software host PC and the Concept M2 control PC. Over this link the stage software interfaces with a corresponding LabVIEW program on the Concept M2 PC to send position commands for each of the scanners.

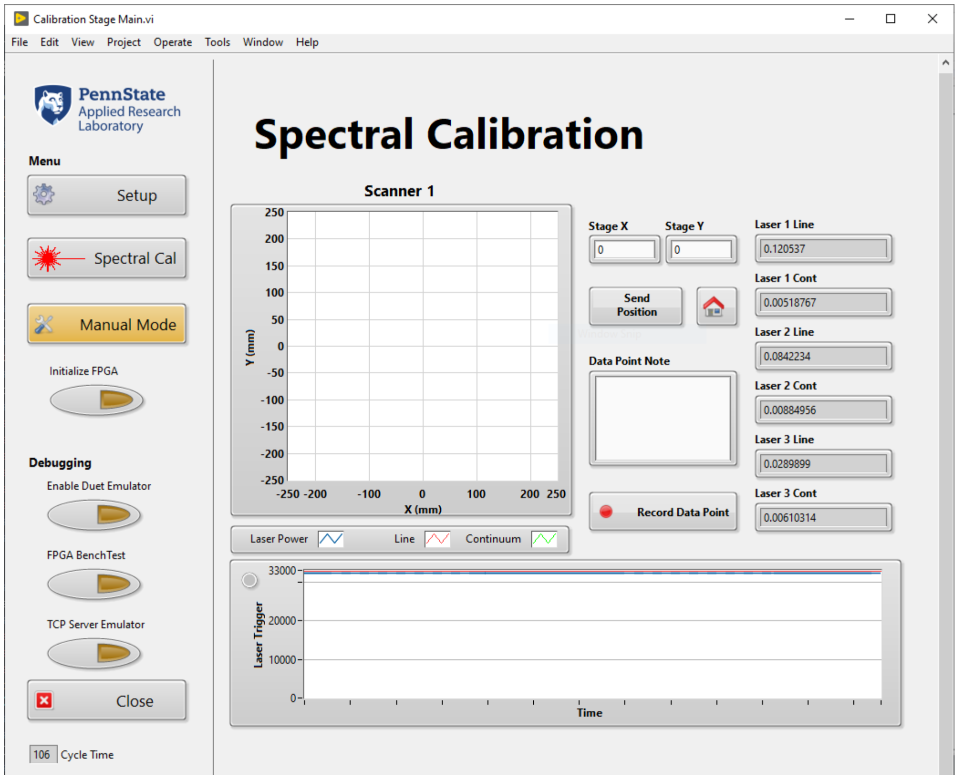

Figure **4-4** Calibration stage control software.

4.3 Applying Calibration Data

This coordination between the two systems allows the stage system to accurately collect spectral data from each of the two spectral sensors. Data is collected at discrete points across a two-dimensional grid which yields a spectral intensity grid such as the one shown in figure 3-13.

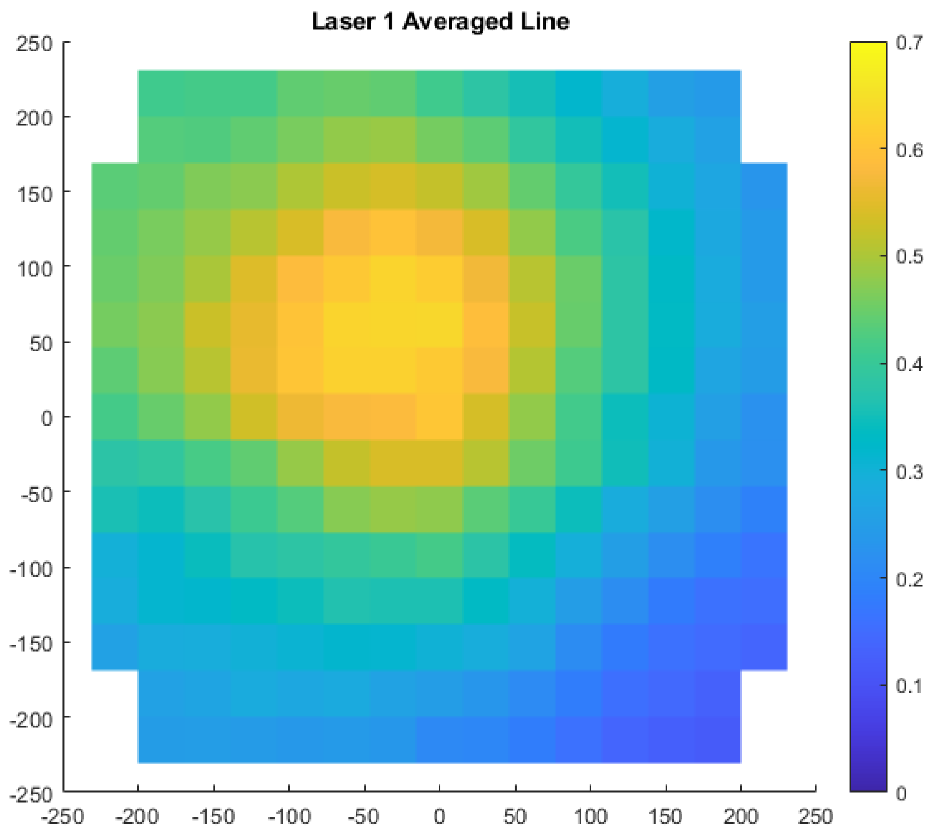

Figure **4-5** Raw spectral calibration data for the line photodiode.

Then, a locally weighted scatter plot smoothing (LOWESS) regression is fit to the discrete 2D data to create a continuous representation of the spatial spectral variation across the build plate.

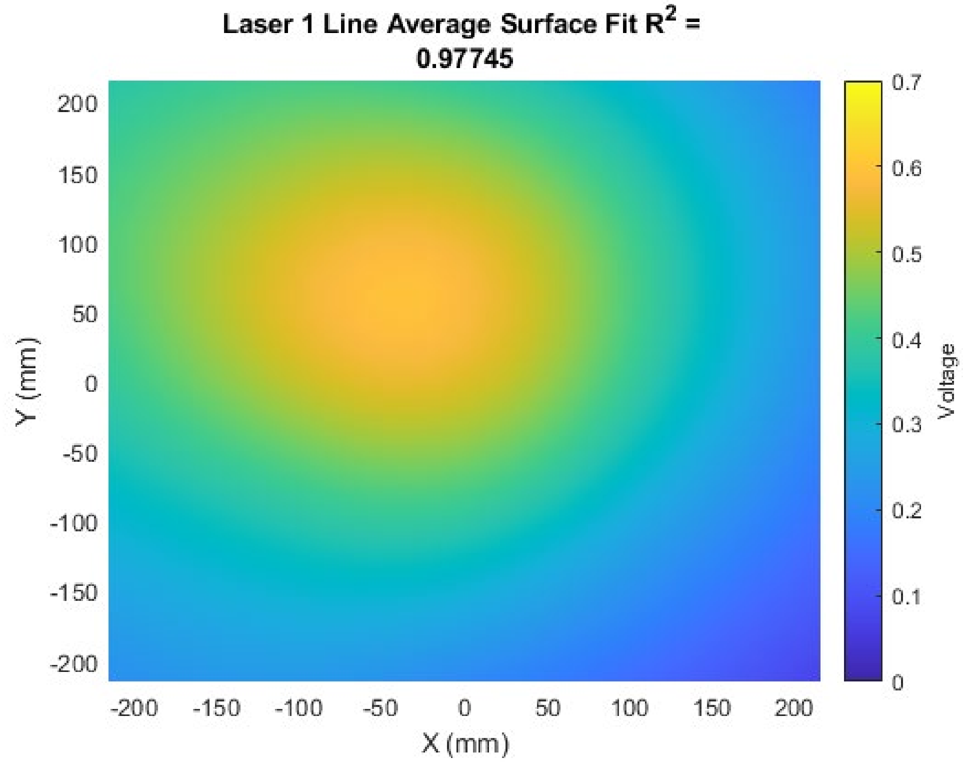

Figure **4-6** Regression surface fit to the spectral calibration data for the line photodiode.

This regression surface can then be used to calibrate data points captured during a build. This is done by first identifying the voltage value on the calibration surface that corresponds to the position of the build data point being calibrated. The calibration voltage value is then inverted by dividing the minimum calibration surface value by the selected positional calibration value. This result is then multiplied to the build data point which yields the calibrated value.

As previously mentioned, the position of the laser beam on the build plate is controlled by the angle of the galvanometer mirrors. As this data shows, the angle of these mirrors has a significant effect on how much light reaches the spectral sensor. This effect results in a spatial variation in spectral intensity independent of the light source intensity. The calibration system was developed to use a light source of a known and constant intensity to quantify the spatial variation in spectral intensity and correct for it. Additionally, the calibration system also has secondary objective to serve as a test bed for using other sensors within a PBFAM system.

Chapter 5

Multi-Spectral Sensor Functionality Experiment

5.1 Objective

The objective of this experiment is to purposely induce the formation of flaws during the LPBFAM process to test the ability of the multi-spectral sensor to detect these flaws. As previously stated, fluctuations in spectral emissions from the plasma plume have been shown to correlate to the existence of build defects in as built parts. Keyhole defects are a subcategory of build flaws that form due to excessive laser energy creating a deep melt pool which has the propensity to result in the formation of trapped gas porosity. In this experiment, keyhole defects are induced in certain parts by decreasing the laser speed and spot diameter. Additional parts are fabricated with nominal build conditions for comparison. Computed tomography (CT) scanning of the built parts was used to quantify the porosity present in each part which was compared against the bulk spectral data captured to determine the relationship between flaw formation and spectral sensor response.

5.2 Build Plan

This experiment was executed using Ti6Al4V powder on a Concept M2 dual laser PBFAM system with multi-spectral sensors installed on both scanner systems. To test the effects of defect formation on spectral response, small test cylinders were distributed across the build plate and assigned to one of two lasers and one of two parameter sets. The cylinder model is shown in figure 5-1.

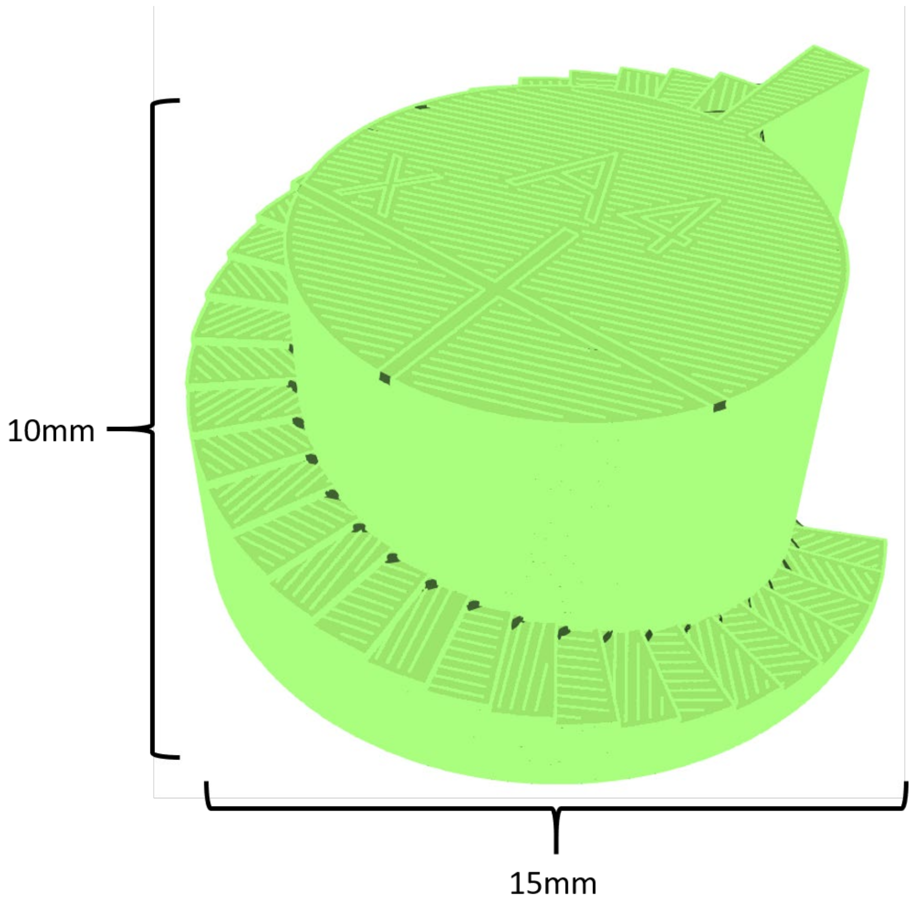

Figure **5-1** Cylinder model used for experimentation.

The build parameters for each cylinder were selected from previous single-track experiments performed on the same system. From this previous experiment, a parameter set that produced ideal weld beads was selected as the nominal condition and a parameter set that produced keyhole defects was selected as the keyhole condition. These two parameter sets are summarized in table 5-1.

Table **5-1** Build parameter sets.

Parameter Set	**Norm. Enthalpy**	**Power [W]**	**Speed [mm/s]**	**Layer height [um]**	**Spot Diameter [um]**	**Hatch Spacing [um]**
Nominal 2	7.9	400	615	100	200	208
Keyhole 2	12.52	350	445	100	150	201

As shown in figure 5-2 the nominal parameter set produces welds with an ideal depth to width ratio while the keyhole parameter set results in a high aspect ratio melt pool which results in the formation of trapped gas porosity.

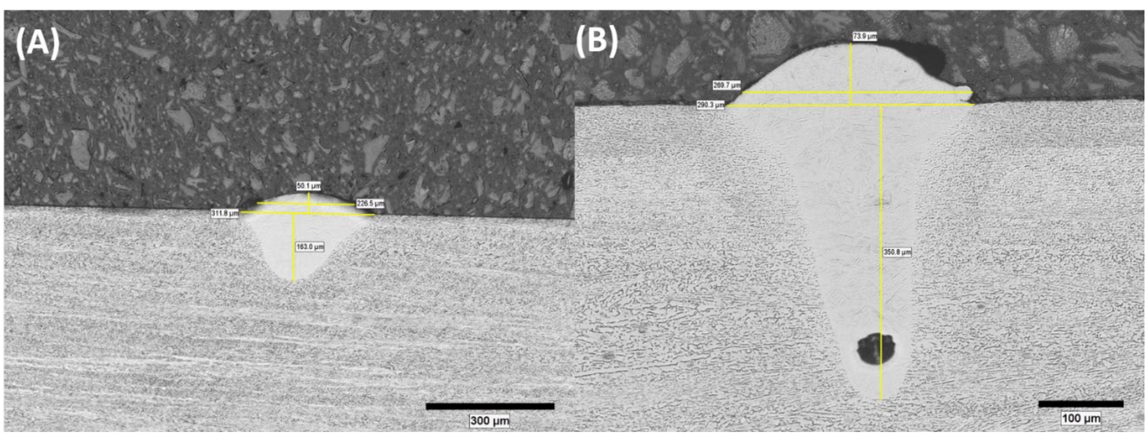

Figure **5-2** (A) Nominal parameter set weld cross section (B) Keyhole parameter set weld cross section.

A total of 24 cylinders were built. 12 cylinders were designated for each laser with each group being split among the nominal and keyhole parameter sets. This layout is shown in figure 5-3.

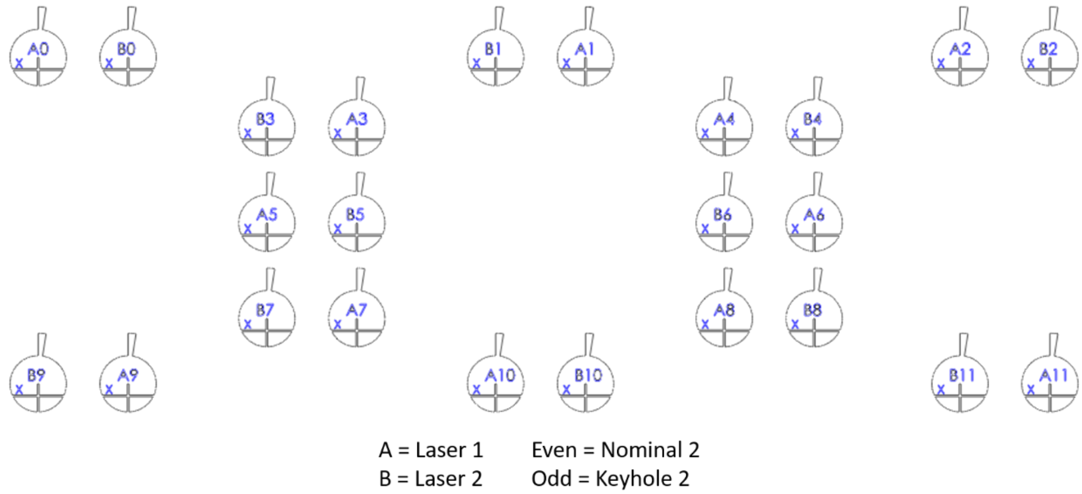

Figure **5-3** Cylinder build layout

The cylinder build was initially designed to be one of three experiments performed in one build, however due to a data recording error, only spectral data from the cylinder experiment was recorded. Because of this, only the cylinder portion of the build will be discussed in this paper.

5.3 Data Processing

Raw data from the multi-spectral sensors, along with scanner position and laser power data is recorded to a database file. Each database file contains the data for a single layer and the name for each file is incremented to indicate the layer number. The raw data is then processed using a file conversion script which performs timing corrections, converts scanner positions to machine coordinates, and exports the data into a new file. This process is shown in figure 5-4. Currently the script is capable of outputting files in Paraview, Matlab, or CSV format. The data discussed herein will be analyzed using Paraview.

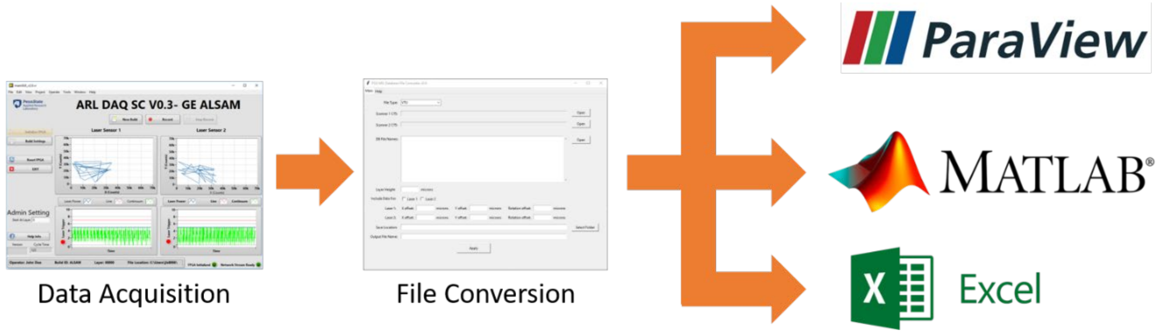

Figure **5-4** Data processing diagram

5.4 Porosity Analysis

Each as-built cylinder was removed from the print bed and analyzed for porosity using a CT scanner. Each cylinder was scanned at a 10-micron voxel resolution and imported into Volume Graphics (VG) studio for further analysis. Using the built in VG Easypore module to identify voids in each component. This was used to determine the total number of flaw voxels present in each cylinder. This data were then compared with the captured spectral data to draw relationships between the presence of flaws and the captured data.

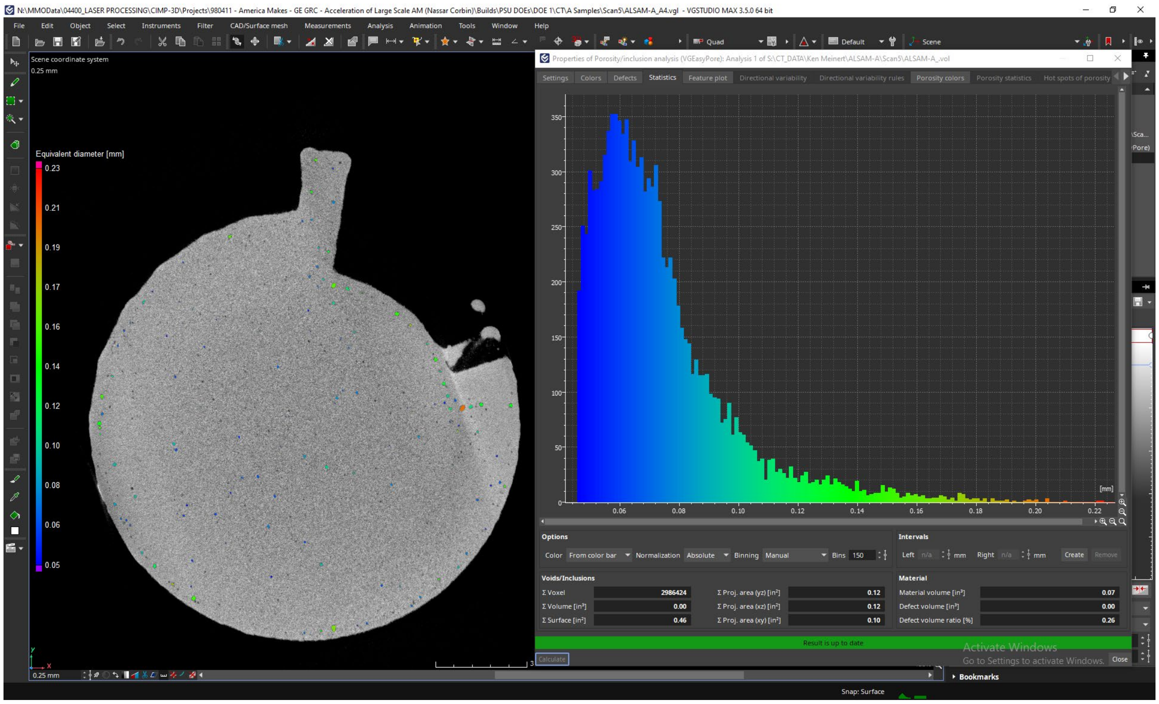

Figure **5-5** Volume Graphics Studio porosity analysis

Chapter 6

Results and Discussion

6.1 Visual Analysis

The as-built parts including the omitted components are shown in figure 6-1. All parts were completed successfully without any failures or build stoppages. The as-built parts were separated from the build plate using an electric discharge machining (EDM) tool and were subsequently analyzed.

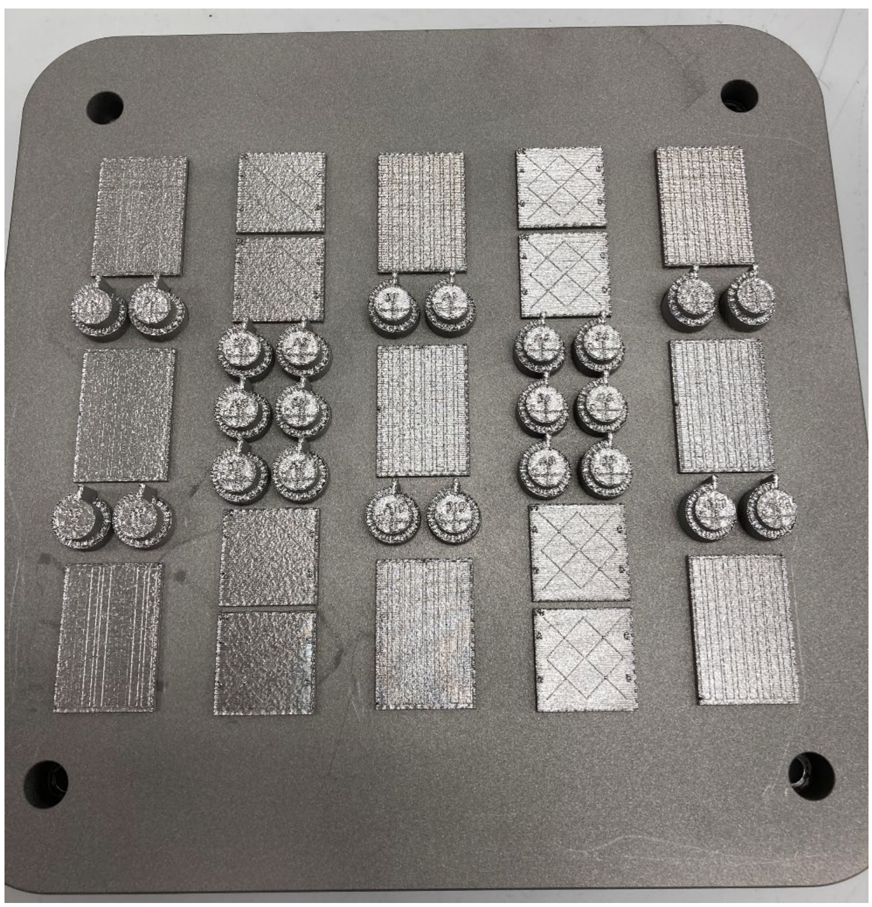

Figure **6-1** Final build including omitted components.

The spectral data captured during this build were reconstructed in Paraview to provide a 3D view of the captured data. This visualization is shown in figure 6-2.

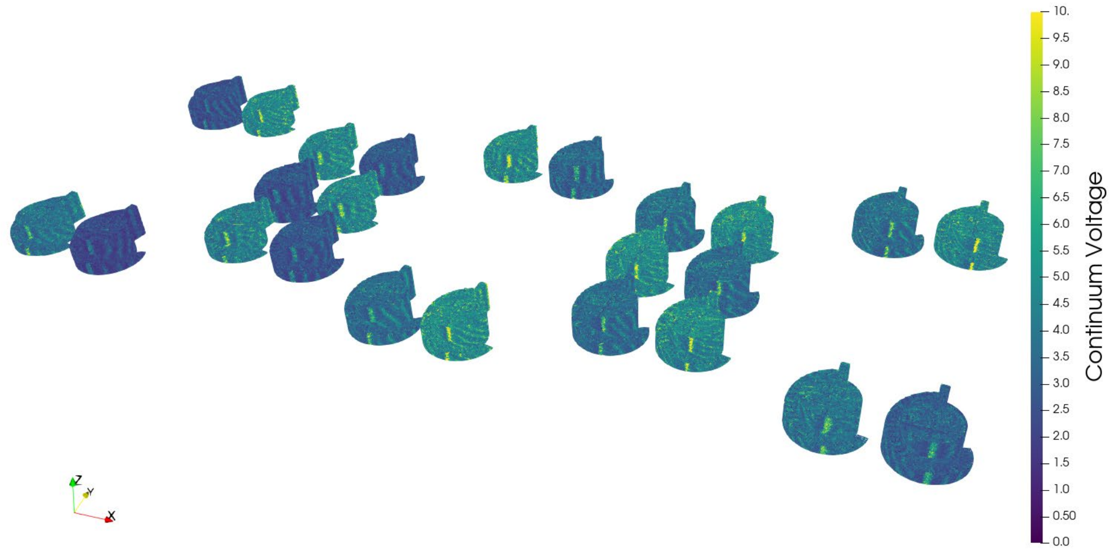

Figure **6-2** 3D visualization of spectral data.

The most notable visual feature exhibited by all components in the build was a periodic change in layer height around all external contours. This height variation resulted from an unstable melt pool size which was likely induced by improper contour parameters. In this build, the contour lasing parameters were kept equal to the hatch parameters instead of using contour-specific parameters. This resulted in an unstable melt pool formation on the contours which built up from layer to layer, forming striations that are visible of the final parts. These striations are shown in figure 6-3.

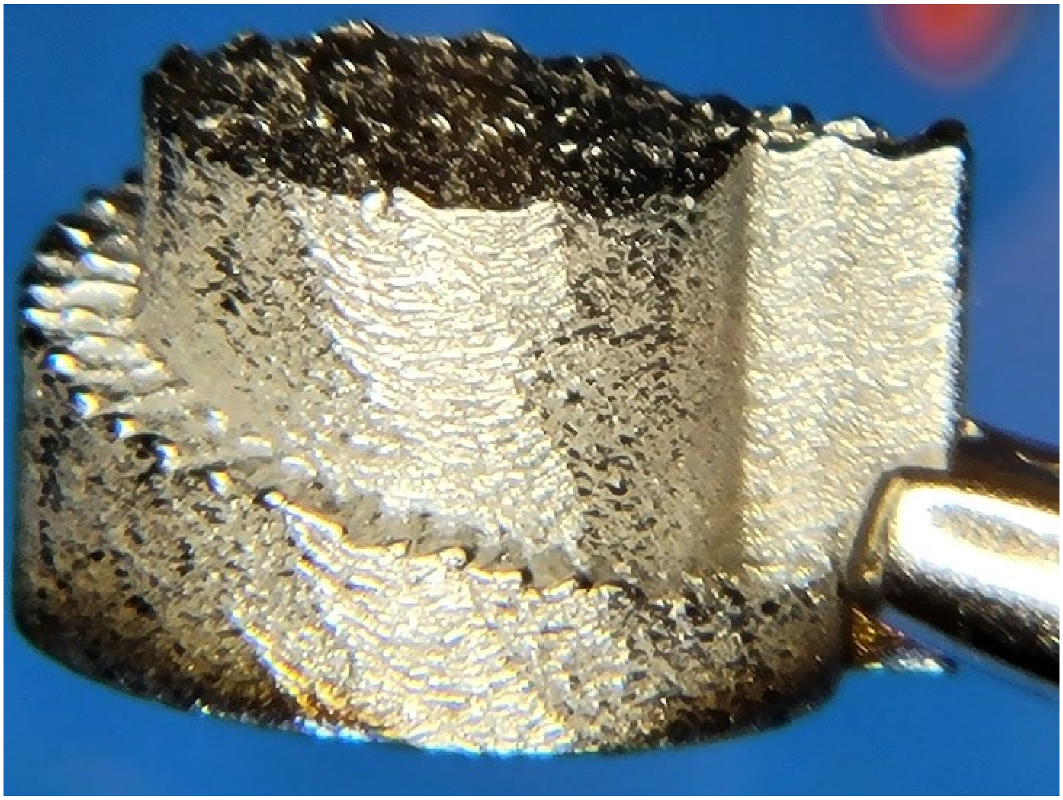

Figure **6-3** Cylinder specimen showing vertical striations resulting from contour melt pool instability.

This melt pool instability resulted in the formation of a fluctuating plasma plume, which is evident in the spectral data presented in figure 6-4. This shows an oscillating spectral response on the contour which corresponds to the striations shown in figure 6-3. This shows that peaks in spectral response correspond with the peaks in melt pool size. In the case of an unstable melt pool, this response is expected as a larger melt pool is expected to produce a larger plasma plume and emit more light.

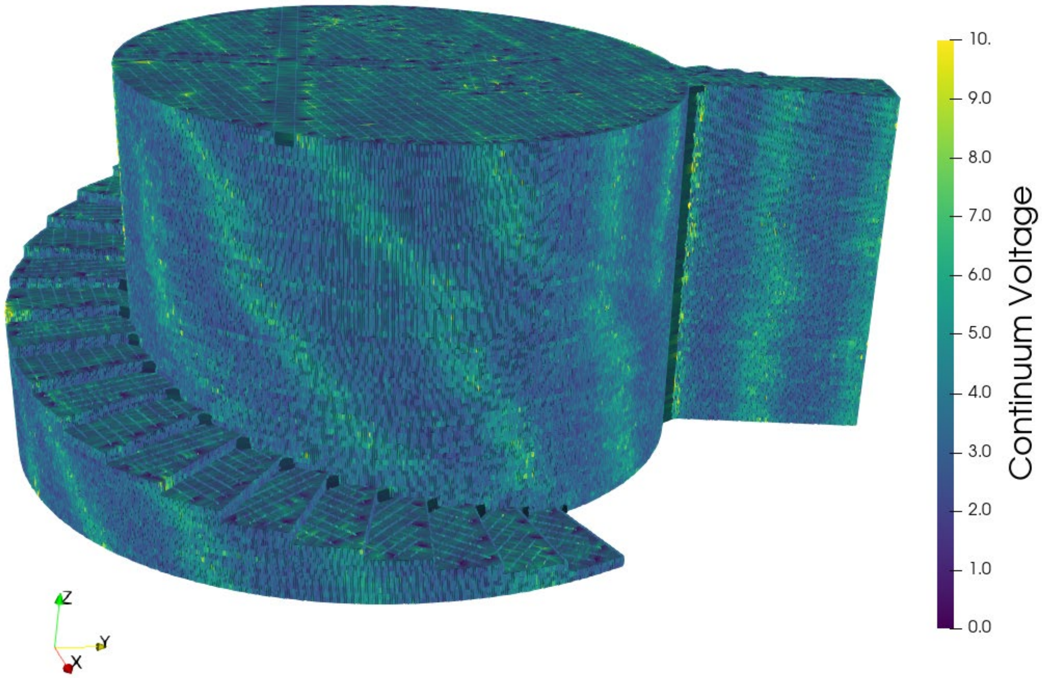

Figure **6-4** The peaks of the melt pool size show up as peaks in raw spectral intensity.

In addition to the oscillating spectral response due to melt pool instabilities, a prominent spectral response formed at the same vertical location on all cylinders which corresponded with the start/stop locations of each contour. This effect can be seen on the left-hand side of figure 6-5.

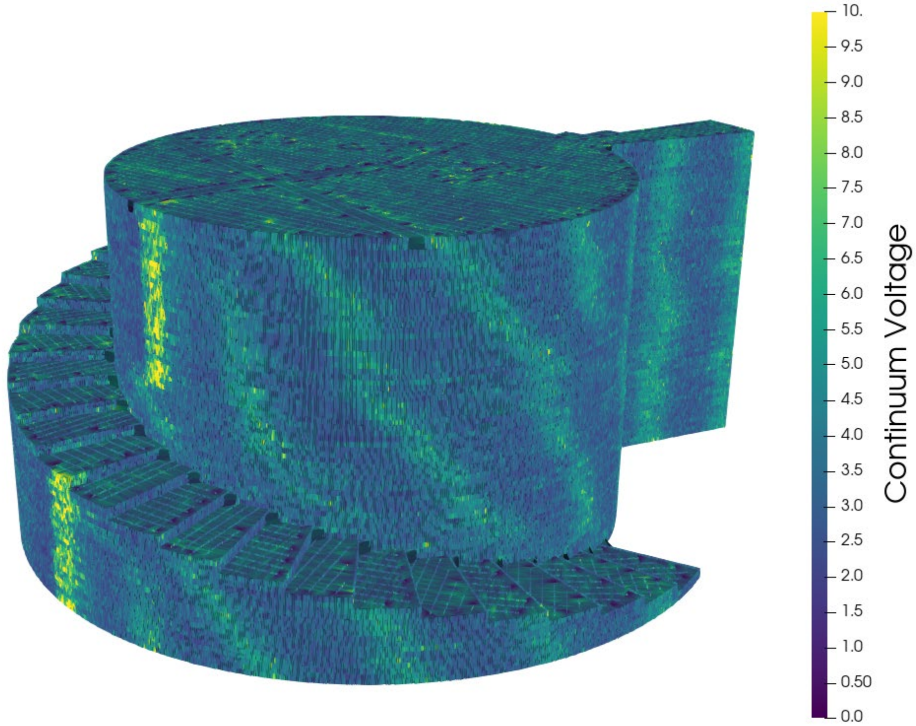

Figure **6-5** Prominent spectral response resulting from the start/stop of each contour.

At the start/stop location for each contour there is a peak in melt pool size corresponding with the other periodic melt pool peaks located around the perimeters of the samples. This periodicity occurs for both the line and continuum sensors but is noticeably amplified for the line photodiode as shown in figure 6-6. This figure compares the photodiode responses for the contours and the hatches. This shows that the contour distributions are wider and possess a significant peak at ten volts due to sensor saturation.

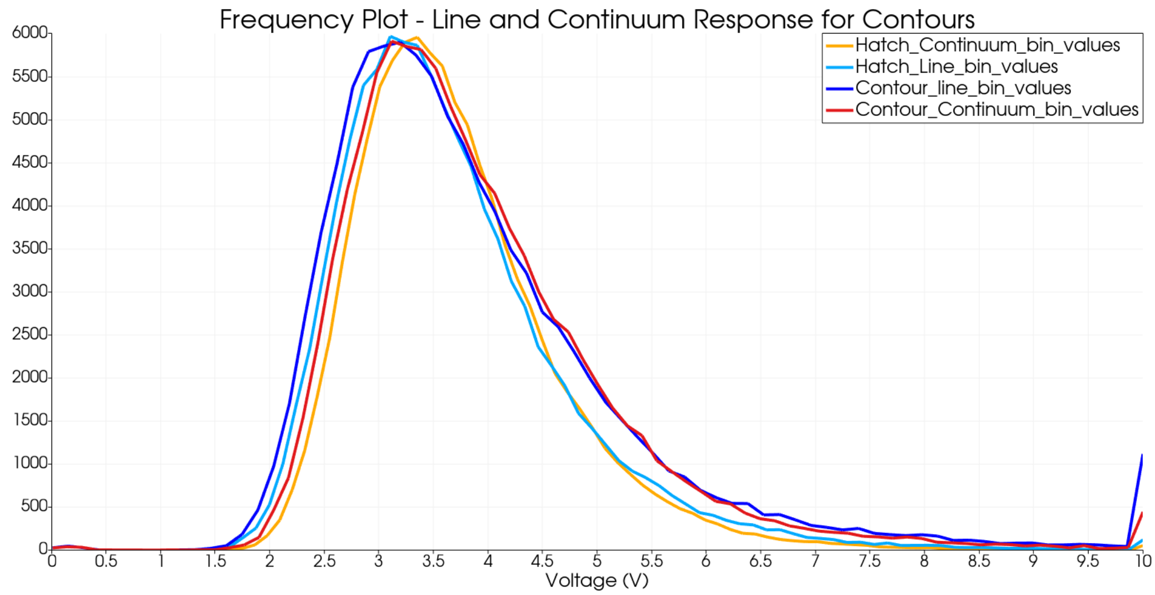

Figure **6-6** Frequency distribution for line and continuum values on contours and hatches.

6.2 Internal Porosity Analysis

CT scan data collected for each sample showed a high degree of porosity present in both the keyhole and nominal cylinders. Example CT data from a cylinder processed under nominal processing parameters and parameters intended to induce keyhole instabilities are shown in figure 6-7 and 6-8 respectively. Such a high degree of porosity in the nominal cylinders was unexpected, however the porosity is significantly less than that of the keyhole cylinders.

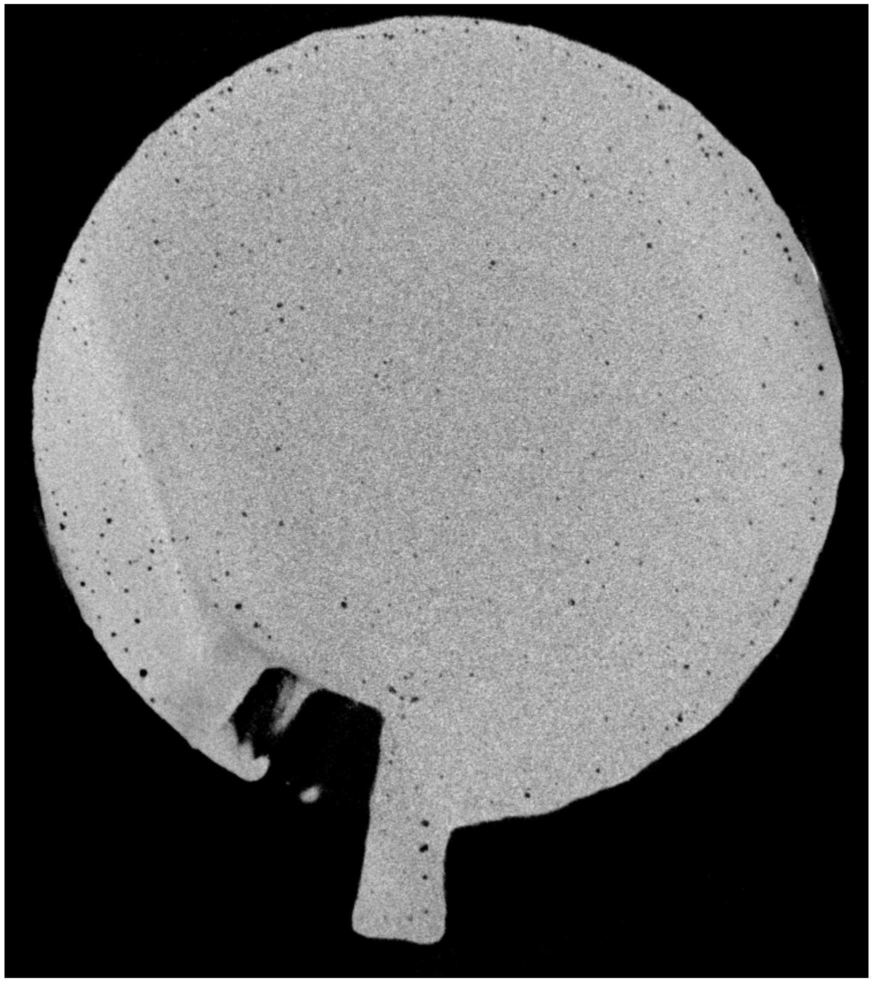

Figure **6-7** XY CT slice from nominal cylinder A4.

In the nominal cylinders, flaws are often located near the part surface, seeming to follow the path of the contour with other flaws randomly situated throughout the volume of the cylinder. Within the keyhole cylinders straight lines of flaws are formed corresponding to the hatching paths.

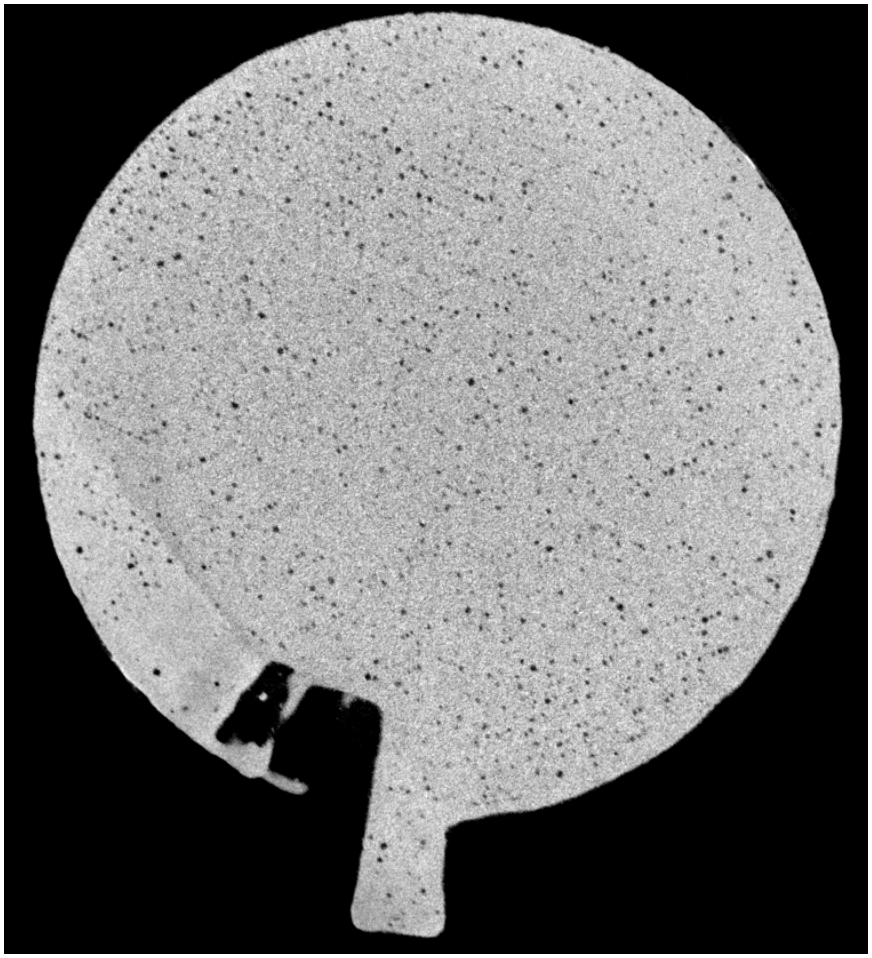

Figure **6-8** XY CT slice from keyhole cylinder A1.

The manufacture of the keyhole cylinders was a success, in that each cylinder contains a high degree of porosity. The nominal cylinders produced less ideal results due to the higher than expected porosity. Despite this the porosity, analysis shows that keyhole cylinders have significantly higher porosity than nominal which is confirmed in figure 6-9. This result was expected and paves the way for further analysis of the spectral data collected during the build.

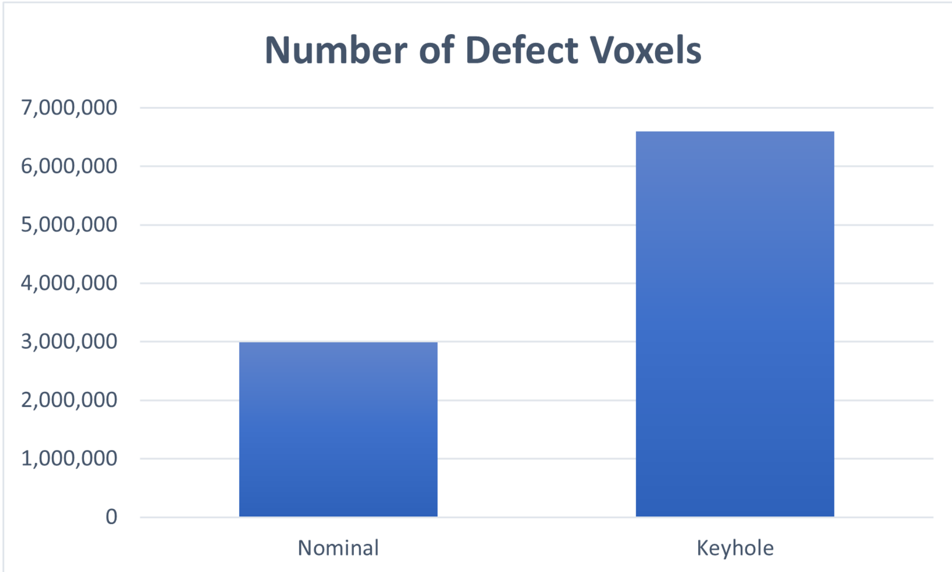

Figure **6-9** Average number of defect voxels (10 micron voxel size) for nominal and keyhole cylinders.

Using the line and continuum signals collected during the build, the line-to-continuum ratio was calculated. The resulting frequency distribution of line-to-continuum values in both the nominal and keyhole cylinders is shown in figure 6-10. These data shows that the average line-to-continuum value for the nominal cylinders is significantly less than that of the keyhole cylinders. Additionally the distribution of line-to-continuum values for the keyhole cylinders is broader than that of the nominal set.

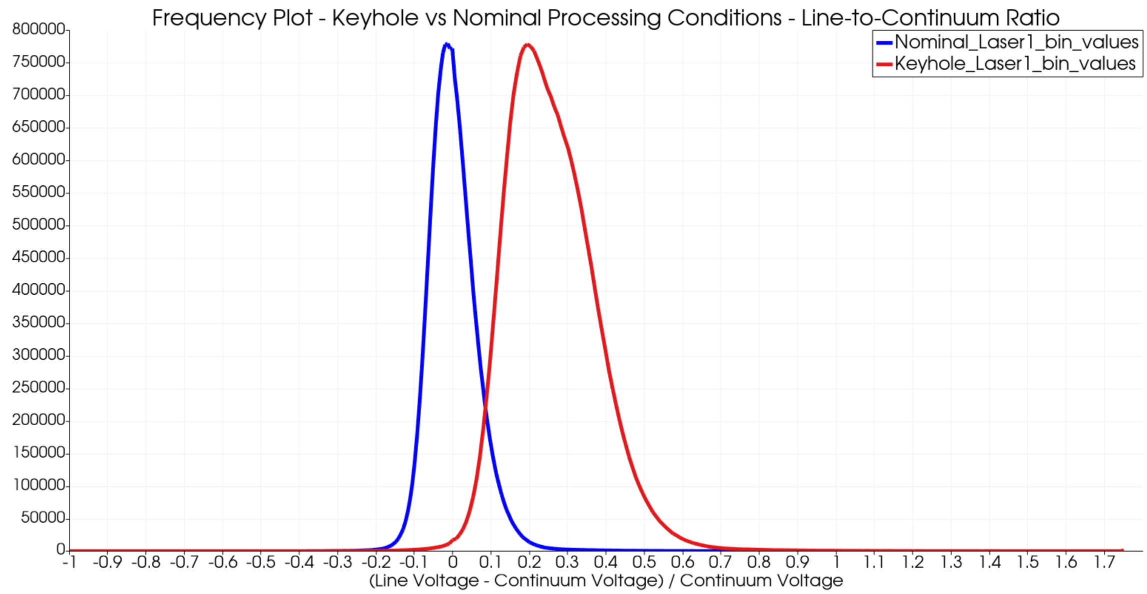

Figure **6-10** Frequency plot for the line-to-continuum ratio associated with both nominal and keyhole cylinders.

These results show that the cylinders with higher degrees of porosity exhibit a higher average line-to-continuum ratio. This analysis was only completed for the spectral data captured from laser one due to the aforementioned saturation in the photodiode signal from the laser two sensor. This saturation leads to erroneous line-to-continuum calculations which do not make it suitable for further analysis.

Chapter 7

Conclusions and Future Work

This work has introduced multi-spectral monitoring method suitable for use in multi-laser PBFAM systems. An on-axis multi-spectral sensor was developed which was paired with an electromechanical stage system designed to assist in calibrating the sensors. To assess the efficacy of using this system as a means to detect the real time formation of flaws in-situ, an experiment was executed to compare the use of nominal processing conditions vs a keyhole condition intended to produce higher levels of bulk porosity. The build specimens produced from this build were subsequently CT scanned and analyzed to quantify the levels of porosity in each part.

While all the part produced during the build experiment exhibited a high degree of porosity, the keyhole samples produced the highest levels of porosity. Void analysis of the CT data confirms that the defect area in the keyhole specimens was approximately double of that for the nominal specimens. Bulk spectral analysis of these parts show that the keyhole specimens exhibit a significantly higher average line-to-continuum ratio than the nominal specimens. This shows a strong correlation between bulk porosity in as-built parts and the line-to-continuum ratio calculated from the spectral data recorded during the build. This agrees with prior research that has shown a correlation between the line-to-continuum and the presence of build defects [2], [19], [31]. This shows that the line-to-continuum ratio provides a valuable insight into the formation of defects in as built parts.

Valuable insight was also gained on how melt pool instability affects the plasma plume formation during the laser welding process. A periodic change in melt pool size along the part contours compounded each layer to form a wavy top surface. The peaks and valleys of the contours caused by this melt pool instability are mirrored by peaks and valleys in the spectral data. This shows that spectral data captured using the line and continuum analysis approach can be used to identify build defects that arise due to melt pool instabilities.

These results show that the on-axis spectral sensing approach developed herein is an effective way to adapt the line and continuum spectral monitoring method for use in multi-laser powder bed fusion systems. This on-axis approach solves the issue of sensing in a multi-laser system, however, it also introduces new challenges and complexities into the overall system. The most significant challenge was compensating for the spatial variation in spectral intensity measured by the spectral sensors. The solution to this problem was the development of a multi-axis electromechanical stage system which moves a lightbulb of a known emission spectrum around the processing plane while data is collected by the spectral sensors. This process yields data that is then used to compensate for the spatial variation in spectral sensor response. It was found during the development of the calibration system that an extremely uniform light source is required to perform an accurate spectral calibration which is difficult to achieve using the halogen bulbs which served as the main calibration light source in this project. Characteristics of the light bulb such as bulb shape and glass opacity were discovered to be significant factors in uniformity of the emitted light. Because the galvanometer scanners are aimed at the light bulb from different angles during the calibration process it is imperative the light emitted from the bulb be as uniform with respect to radiance angle. To determine if a light bulb is an acceptable calibration light source, future work should include the characterization of light sources using a spectrophotometer to determine how uniform the emitted light is. Future work should also investigate the use of LED’s with high color rendering indices (CRI’s) to determine if they are a suitable candidate to replace the halogen bulbs used as calibration light sources in this paper. The use of LED’s would allow for the development of a completely solid-state calibration system, replacing the current electromechanical stage system with a single PCB containing an array of LED’s. This approach would lower costs, increase usability, and increase the positional accuracy of the calibration system. It is also worth investigating whether the use of the reflectivity data of the galvanometer mirrors captured using a spectrophotometer could be used to create an accurate simulation of the spatial variation in spectral intensity. This approach could potentially remove the need for an external calibration system altogether.

What has been shown in this work is the ability to use in-situ spectroscopy-based sensing data to determine the relative presence of bulk porosity in parts fabricated via PBFAM. Further research is required to determine the efficacy of using this method to determine if this approach is applicable for identifying the location of individual defects. This requires the position of individual flaws to be compared against the local spectral data to determine if any correlations exist. A key result found from the experiment was the high levels of porosity in the nominal cylinders. Even though the porosity was less than that of the keyhole cylinders it was still a significant presence and is therefore desirable to detect. Further research into the spectral response received from the manufacture of relatively error free parts is needed to determine if the current spectral sensing system can make such determinations.

This work builds upon a photodiode based spectral sensing approach established in prior research to adapt it for use in multi-laser powder bed fusions systems. The experimental results show that the on-axis spectral sensing system developed herein is an effective approach for identifying build defects such as trapped gas porosity and melt pool instabilities that can form during the metal powder bed fusion process. The use of this sensing approach is therefore a good candidate in the future for the real time detection of build defects to help accelerate the qualification of components manufactured via PBFAM.

References

[1] B. K. Foster, E. W. Reutzel, A. R. Nassar, C. J. Dickman, and B. T. Hall, “A brief survey of sensing for metal-based powder bed fusion additive manufacturing,” in *Dimensional Optical Metrology and Inspec tion for Practical Applications IV*, May 2015, vol. 9489, no. 14, p. 94890B, doi: 10.1117/12.2180654.

[2] A. R. Nassar, T. J. Spurgeon, and E. W. Reutzel, “Sensing defects during directed-energy additive manufacturing of metal parts using optical emissions spectroscopy,” in *25th Annual International Solid Freeform Fabrication Symposium &#65533; An Additive Manufacturing Conference, SFF 2014*, 2014, pp. 278–287.

[3] A. J. Dunbar and A. R. Nassar, “Assessment of optical emission analysis for in-process monitoring of powder bed fusion additive manufacturing,” *Virtual Phys. Prototyp.*, vol. 13, no. 1, pp. 14–19, Jan. 2018, doi: 10.1080/17452759.2017.1392683.

[4] Z. Snow, A. R. Nassar, and E. W. Reutzel, “Invited Review Article: Review of the formation and impact of flaws in powder bed fusion additive manufacturing,” *Additive Manufacturing*, vol. 36. Elsevier B.V., p. 101457, Dec. 01, 2020, doi: 10.1016/j.addma.2020.101457.

[5] S. Katayama, Y. Kawahito, and M. Mizutani, “Collaboration of physical and metallurgical viewpoints for understanding and process development of laser welding,” in *26th International Congress on Applications of Lasers and Electro-Optics, ICALEO 2007 - Congress Proceedings*, Sep. 2007, vol. 2007, no. 1, p. 701, doi: 10.2351/1.5061089.

[6] A. Kramida, Y. Ralchenko, and J. Reader, “NIST Atomic Spectra Database (ver. 5.8),” *National Institute of Standards and Technology*, 2020. https://physics.nist.gov/asd (accessed Jun. 09, 2021).

[7] “New manufacturing milestone: 30,000 additive fuel nozzles | GE Additive.” https://www.ge.com/additive/stories/new-manufacturing-milestone-30000-additive-fuel-nozzles (accessed May 25, 2021).

[8] “Statistics on Global 3D Printing Metals Market Size Will.” https://www.globenewswire.com/news-release/2021/03/03/2186136/0/en/Statistics-on-Global-3D-Printing-Metals-Market-Size-Will-Reach-USD-5167-9-Million-By-2026-Facts-Factors.html (accessed May 25, 2021).

[9] “M2 series 5 | GE Additive.” https://www.ge.com/additive/additive-manufacturing/machines/m2series5 (accessed May 25, 2021).

[10] G. Tapia and A. Elwany, “A Review on Process Monitoring and Control in Metal-Based Additive Manufacturing,” *Journal of Manufacturing Science and Engineering, Transactions of the ASME*, vol. 136, no. 6. American Society of Mechanical Engineers (ASME), Dec. 01, 2014, doi: 10.1115/1.4028540.

[11] C. B. Stutzman, A. R. Nassar, and E. W. Reutzel, “Multi-sensor investigations of optical emissions and their relations to directed energy deposition processes and quality,” *Addit. Manuf.*, vol. 21, pp. 333–339, May 2018, doi: 10.1016/j.addma.2018.03.017.

[12] H. Sebestova, H. Chmelickova, L. Nozka, and J. Moudry, “Non-destructive real time monitoring of the laser welding process,” *J. Mater. Eng. Perform.*, vol. 21, no. 5, pp. 764–769, May 2012, doi: 10.1007/s11665-012-0193-4.

[13] W. M. Steen and J. Mazumder, *Laser material processing: Fourth edition*. Springer London, 2010.

[14] A. Sun, E. Kannatey-Asibu, and M. Gartner, “Sensor systems for real-time monitoring of laser weld quality,” *J. Laser Appl.*, vol. 11, no. 4, pp. 153–168, Aug. 1999, doi: 10.2351/1.521893.

[15] D. Hu and R. Kovacevic, "Sensing, modeling and control for laser-based additive manufacturing," *Int. J. Mach. Tools Manuf.*, vol. 43, no. 1, pp. 51–60, Jan. 2003, doi: 10.1016/S0890-6955(02)00163-3.

[16] T. Craeghs, F. Bechmann, S. Berumen, and J. P. Kruth, "Feedback control of Layerwise Laser Melting using optical sensors," in *Physics Procedia*, Jan. 2010, vol. 5, no. PART 2, pp. 505–514, doi: 10.1016/j.phpro.2010.08.078.

[17] B. Lane *et al.*, "Measurements of Melt Pool Geometry and Cooling Rates of Individual Laser Traces on IN625 Bare Plates," vol. 9, 2020, doi: 10.1007/s40192-020-00169-1.

[18] S. K. Everton, M. Hirsch, P. I. Stavroulakis, R. K. Leach, and A. T. Clare, "Review of in-situ process monitoring and in-situ metrology for metal additive manufacturing," *Materials and Design*, vol. 95. Elsevier Ltd, pp. 431–445, Apr. 05, 2016, doi: 10.1016/j.matdes.2016.01.099.

[19] A. Ancona, V. Spagnolo, P. M. Lugarà, and M. Ferrara, "Optical sensor for real-time monitoring of CO_2 laser welding process," *Appl. Opt.*, vol. 40, no. 33, p. 6019, Nov. 2001, doi: 10.1364/ao.40.006019.

[20] D. Y. You, X. D. Gao, and S. Katayama, "Review of laser welding monitoring," *Sci. Technol. Weld. Join.*, vol. 19, no. 3, pp. 181–201, 2014, doi: 10.1179/1362171813Y.0000000180.

[21] P. B. Garcia-Allende, J. Mirapeix, O. M. Conde, A. Cobo, and J. M. Lopez-Higuera, "Defect detection in arc-welding processes by means of the line-to-continuum method and feature selection," *Sensors*, vol. 9, no. 10, pp. 7753–7770, Oct. 2009, doi: 10.3390/s91007753.

[22] A. Sun, E. Kannatey-Asibu, and M. Gartner, "Monitoring of laser weld penetration using sensor fusion," *J. Laser Appl.*, vol. 14, no. 2, pp. 114–121, May 2002, doi: 10.2351/1.1471562.

[23] T. Sibillano *et al.*, "Spectroscopic closed loop control of penetration depth in laser beam welding process," in *High Power Laser Materials Processing: Lasers, Beam Delivery, Diagnostics, and Applications*, Feb. 2012, vol. 8239, p. 82390S, doi: 10.1117/12.906778.

[24] M. Montazeri, A. R. Nassar, A. J. Dunbar, and P. Rao, "In-process monitoring of porosity in additive manufacturing using optical emission spectroscopy," *IISE Trans.*, vol. 52, no. 5, pp. 500–515, May 2020, doi: 10.1080/24725854.2019.1659525.

[25] William M. Steen and Jyotirmoy Mazumder, *Laser Material Processing*, 4th ed. Springer, 2010.

[26] K. Chaudhary, S. Z. H. Rizvi, and J. Ali, "Laser-Induced Plasma and its Applications," in *Plasma Science and Technology - Progress in Physical States and Chemical Reactions*, InTech, 2016.

[27] H. R. Griem, "Principles of Plasma Spectroscopy," in *Fast Electrical and Optical Measurements*, Springer Netherlands, 1986, pp. 885–910.

[28] P. B. Garcia-Allende, J. Mirapeix, O. M. Conde, A. Cobo, and J. M. Lopez-Higuera, "Defect detection in arc-welding processes by means of the line-to-continuum method and feature selection," *Sensors*, vol. 9, no. 10, pp. 7753–7770, Oct. 2009, doi: 10.3390/s91007753.

[29] J. Mirapeix, R. Ruiz-Lombera, J. J. Valdiande, L. Rodriguez-Cobo, F. Anabitarte, and A. Cobo, "Defect detection with CCD-spectrometer and photodiode-based arc-welding monitoring systems," *J. Mater. Process. Technol.*, vol. 211, no. 12, pp. 2132–2139, Dec. 2011, doi: 10.1016/j.jmatprotec.2011.07.011.

[30] S. Katayama, Y. Kawahito, and M. Mizutani, "Elucidation of laser welding phenomena and factors affecting weld penetration and welding defects," in *Physics Procedia*, Jan. 2010, vol. 5, no. PART 2, pp. 9–17, doi: 10.1016/j.phpro.2010.08.024.

[31] A. J. Dunbar and A. R. Nassar, “Assessment of optical emission analysis for in-process monitoring of powder bed fusion additive manufacturing, Virtual and Physical Prototyping,” vol. 13, no. 1, pp. 14–19, 2018, doi: 10.1080/17452759.2017.1392683.

Appendix A

Build Experiment Images

1. Cylinder close up:

2. Contour waviness due to melt pool instability:

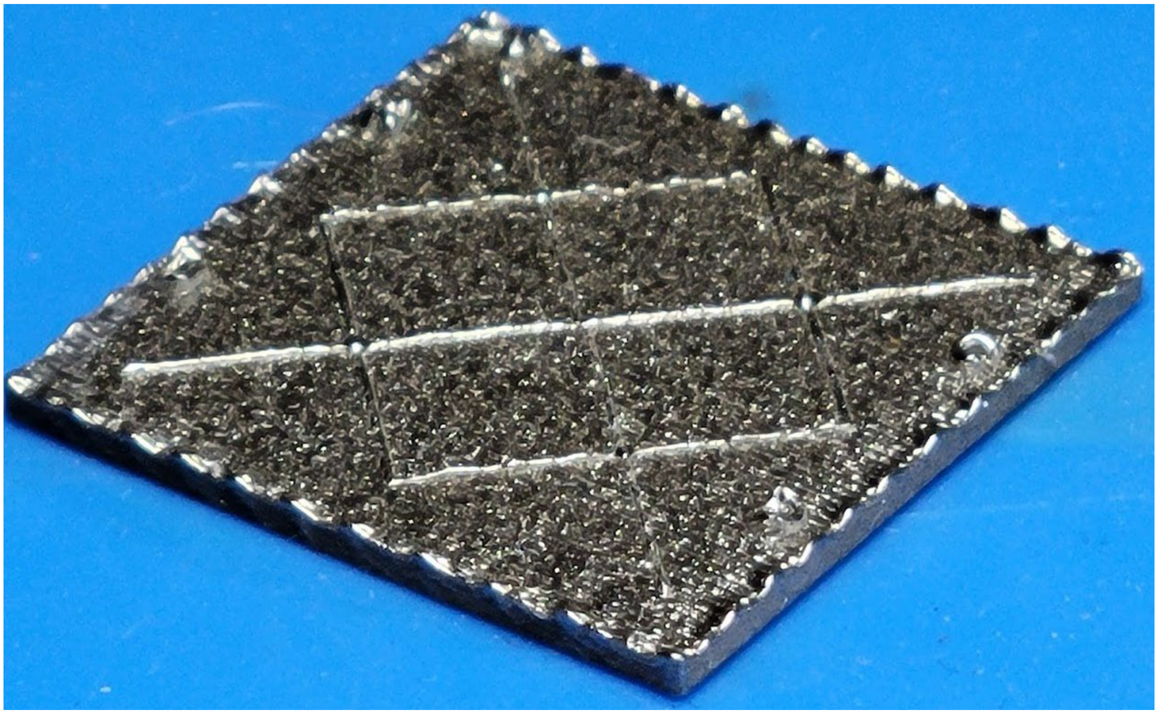

3. Cylinder grouping:

Appendix B

Reconstructed Spectral Data Images

1. Nominal cylinder A4 continuum voltage:

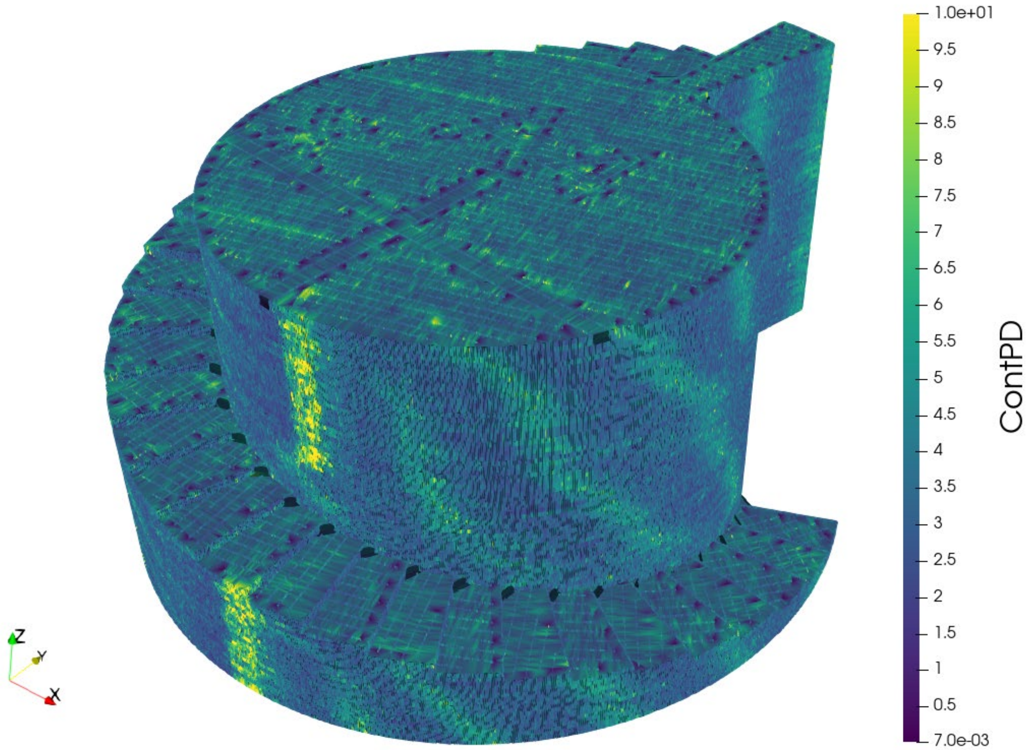

2. Nominal cylinder A4 line voltage:

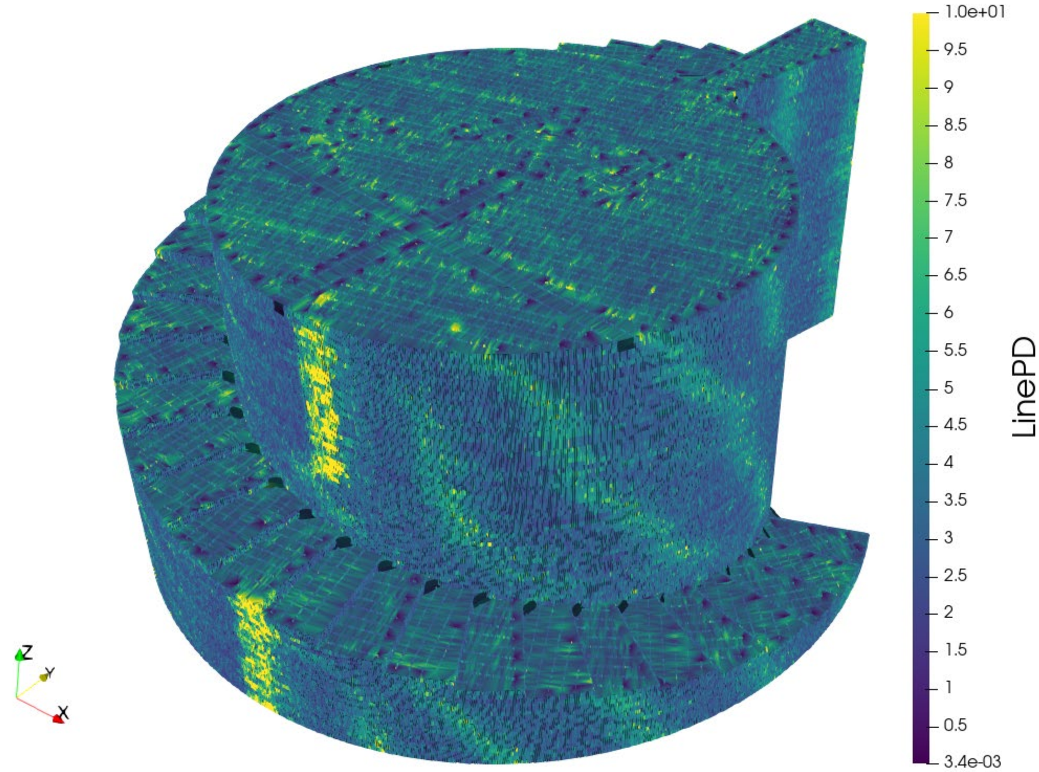

3. Nominal cylinder A4 line-to-continuum ratio